



UNIVERSITY OF SUSSEX

1

DOCTORAL THESIS

2

⁴ Optimisation studies and background
⁵ estimation in searches for the supersymmetric
⁶ partner of the top quark in all-hadronic final
⁷ states with the ATLAS Detector at the LHC

8

9 *A thesis submitted in fulfillment of the requirements*
10 *for the degree of Doctor of Philosophy*

11

in the

12

Experimental Particle Physics Research Group

School of Mathematical and Physical Sciences

Author:

14

Fabrizio MIANO

Supervisor:

14

Dr. Fabrizio SALVATORE

15

24th November 2017

Dedicated to my family.

*Have no fear for atomic energy
'cause none of them can stop the
time*

17

Robert Nesta Marley

18

Acknowledgments

- 19 Thanks to every single thing that went wrong. It made me stronger.

Declaration

21 I, Fabrizio MIANO, hereby declare that this thesis, titled, "Optimisation studies and back-
22 ground estimation in searches for the supersymmetric partner of the top quark in all-
23 hadronic final states with the ATLAS Detector at the LHC" has not been and will not be,
24 submitted in whole or in part to another University for the award of any other degree.

25 *Brighton, 24th November 2017*

University of Sussex
School of Mathematical and Physical Sciences
Experimental Particle Physics Research Group

Doctoral Thesis

31
32 Optimisation studies and background estimation in searches for
33 the supersymmetric partner of the top quark in all-hadronic final
34 states with the ATLAS Detector at the LHC

36 by Fabrizio Miano

Abstract

38 This thesis presents searches for supersymmetry in $\sqrt{s} = 13$ TeV proton-proton collisions
39 at the LHC using data collected by the ATLAS detector in 2015, 2016 and 2017. Events
40 with 4 or more jets and missing transverse energy were selected. Kinematic variables were
41 investigated and optimisations were performed to increase the sensitivity to supersym-
42 metric signals. Standard Model backgrounds were estimated by means of Monte Carlo
43 simulations and data-driven techniques. Before analysing the data in the blinded signal
44 regions the agreement between data and background predictions and the extrapolations
45 from control and validation regions to signal regions were validated. The analysis yiel-
46 ded no significant excess in any of the analyses performed. Therefore limits were set and
47 the results were interpreted as lower bounds on the masses of supersymmetric particles
48 in various scenarios and models.

⁴⁹ Contents

⁵⁰	Introduction	1
⁵¹	1 The Standard Model of particle physics and Supersymmetry	2
⁵²	1.1 The Standard Model	2
⁵³	1.1.1 Electroweak Symmetry Breaking and the Higgs mechanism	6
⁵⁴	1.1.2 Limitations of the Standard Model	9
⁵⁵	1.2 Supersymmetry	11
⁵⁶	1.2.1 Why SUSY?	11
⁵⁷	1.2.2 Minimal Supersymmetric Standard Model	12
⁵⁸	1.2.3 Phenomenology of Supersymmetry	15
⁵⁹	2 The ATLAS Experiment at the LHC	20
⁶⁰	2.1 The LHC	20
⁶¹	2.2 The ATLAS Detector	23
⁶²	2.2.1 The Magnet System	24
⁶³	2.2.2 The Inner Detector	25
⁶⁴	2.2.3 The Calorimeters	28
⁶⁵	2.2.4 The Muon Spectrometer	29
⁶⁶	2.3 The ATLAS Trigger System	30
⁶⁷	3 The ATLAS Trigger System	33
⁶⁸	3.1 Overview	33
⁶⁹	3.1.1 Level 1 Trigger	34
⁷⁰	3.1.2 High-Level Trigger	35
⁷¹	3.2 The tracking	35
⁷²	3.3 Performance of HLT	35
⁷³	3.3.1 Electrons	35
⁷⁴	3.3.2 Muons	35

75	3.3.3 <i>b</i> -jets	35
76	4 Event Simulation and Reconstruction	36
77	4.1 Event Simulation	36
78	4.1.1 Event Generation	36
79	4.1.2 Detector Simulation	36
80	4.2 Object Reconstruction	36
81	4.2.1 Tracks and vertices	37
82	4.2.2 Electrons	37
83	4.2.3 Muons	37
84	4.2.4 Jets	37
85	4.2.5 Missing Transverse Energy	37
86	4.2.6 Overlap Removal	37
87	5 Stop searches in final states with jets and missing transverse energy	38
88	6 Results and Statistical Interpretations	39
89	Appendix A	40
90	Bibliography	41

91 List of Tables

92	1.1 Forces and mediators described by the SM	6
93	1.2 SUSY particles in the MSSM	15
94	1.3 Parameters in the pMSSM.	17

List of Figures

<p>95 List of Figures</p> <p>96 1.1 The elementary particles of the Standard Model. From the outermost to the 97 innermost; fermions (quarks, top-half wheel, leptons, bottom-half wheel), 98 vector bosons, and the Higgs boson.</p> <p>99 1.2 The Higgs potential in the complex plane.</p> <p>100 1.3 Summary of several Standard Model total production cross-section mea- 101 surements, corrected for leptonic branching fractions, compared to the cor- 102 responding theoretical expectations. All theoretical expectations were cal- 103 culated at NLO or higher. The luminosity used for each measurement is 104 indicated close to the data point. Uncertainties for the theoretical predic- 105 tions are quoted from the original ATLAS papers. They were not always 106 evaluated using the same prescriptions for PDFs and scales. Not all mea- 107 surements are statistically significant yet [1].</p> <p>108 1.4 One-loop quantum corrections to the Higgs mass. A fermion correction 109 with coupling λ_f.</p> <p>110 1.5 The inverse couplings of electromagnetic (dashed blue), weak (dashed red) 111 and strong (solid green) interactions with the SM (left) and a supersymmet- 112 ric model (right). In the SM the three lines do not meet at one point, but 113 with the introduction of supersymmetry, and assuming that the supersym- 114 metric particles are not heavier than about 1 TeV, they do meet. This is an 115 indication that supersymmetry could be discovered at the LHC.</p> <p>116 1.6 NLO+NLL production cross-sections as a function of mass at $\sqrt{s} = 13\text{TeV}$ [2]</p> <p>117 1.7 Illustration of stop decay modes in the $(m_{\tilde{t}_1}, m_{\tilde{\chi}_1^0})$ mass place where the $\tilde{\chi}_1^0$ is 118 assumed to be the lightest supersymmetric particle. The dashed blue lines 119 indicate thresholds separating regions where different processes dominate.</p>	<p>3</p> <p>8</p> <p>9</p> <p>10</p> <p>12</p> <p>18</p> <p>18</p>
---	--

120	1.8 Diagrams of the decay topologies of the signal models considered in this	
121	work. The term “soft” refers to decay products that have transverse mo-	
122	menta below the detector thresholds.	19
123	2.1 CERN Accelerator complex. The LHC is the last ring (dark grey line). Smal-	
124	ler machines are used for early-stage acceleration and also to provide beams	
125	for other experiments [3].	22
126	2.2 Cut-away view of the ATLAS detector. The dimensions of the detector are	
127	25 m in height and 44 m in length. The overall weight of the detector is	
128	approximately 7000 tonnes [3].	23
129	2.3 The ATLAS magnet system.	25
130	2.4 The ATLAS Inner Detector	26
131	2.5 A computer generated image of the full calorimeter.	28
132	2.6 Cut-away view of the ATLAS muon system [4].	30
133	2.7 The ATLAS TDAQ system. L1Topo and FTK have not been used for the	
134	results shown in this thesis [5].	31
135	3.1 An Electron-trigger chain (from [6]).	34

¹³⁶ Introduction

¹³⁷ Last thing to write

¹³⁸ **1** | ¹³⁹ **The Standard Model of particle physics and Supersymmetry**

¹⁴⁰

A theory is something nobody believes, except the person who made it. An experiment is something everybody believes, except the person who made it.

Albert Einstein

¹⁴¹ In this chapter, an overview of the Standard Model (SM) of particle physics will be
¹⁴² presented in Section 1.1 together with its limitations in Section 1.1.2 and the need of an ex-
¹⁴³ tension. One of the most popular, supersymmetry, will be discussed in Section 1.2 where,
¹⁴⁴ an overview of the theory, together with the motivations behind its success, will be presen-
¹⁴⁵ ted in Section 1.2.1, followed by the description of the Minimal Supersymmetric Standard
¹⁴⁶ Model (MSSM) in Section 1.2.2, and finally, the phenomenology of supersymmetry, with
¹⁴⁷ particular attention on third-generation supersymmetry, as it is the most relevant theor-
¹⁴⁸ etical support to the analyses presented in this work, will be discussed in Section 1.2.3.

¹⁴⁹ **1.1 The Standard Model**

¹⁵⁰ The SM is an effective theory that aims to provide a general description of fundamental
¹⁵¹ particles and their interactions. Unfortunately, our understanding of nature is still limited
¹⁵² due to some opened question the SM is not able to answer to.

¹⁵³ The 20th century can be considered a quantum revolution. Several experiments led to
¹⁵⁴ discoveries which were found to be, together with the formalised theory, a solid base of
¹⁵⁵ the Standard Model of particle physics and our description of nature. Several particles
¹⁵⁶ were first predicted and then experimentally observed e. g. the W and the Z bosons, the τ

¹⁵⁷ lepton, [7], and more recently the Higgs boson at the LHC discovered by ATLAS [8] and
¹⁵⁸ CMS [9].

¹⁵⁹ The SM is a Quantum Field Theory
¹⁶⁰ (QFT) where particles are treated like ex-
¹⁶¹ citations of quantum fields in a four-
¹⁶² dimensional Minkowski spacetime. It can
¹⁶³ describe three of the four fundamental
¹⁶⁴ forces; weak, electromagnetic, and strong,
¹⁶⁵ but not gravity.

¹⁶⁶ The most general classification of the
¹⁶⁷ elementary particles within the SM can
¹⁶⁸ be made by means of spin and their be-
¹⁶⁹ haviour under Poincaré transformations:
¹⁷⁰ *fermions* (leptons and quarks), usually re-
¹⁷¹ ferred to as matter, which have half-integer
¹⁷² spin values, in unit of \hbar , and *bosons*, usu-
¹⁷³ ally referred to as information carriers,
¹⁷⁴ which have integer-spin values. A note-
¹⁷⁵ worthy subset of bosons is formed by the
¹⁷⁶ Spin-1 bosons, also known as gauge bosons. These can be considered mediators of the
¹⁷⁷ forces. Figure 1.1 displays the elementary particles of the Standard Model known as of
¹⁷⁸ today.

¹⁷⁹ Symmetries and Gauge Groups

¹⁸⁰ In 1915, the German mathematician and theoretical physicist Emmy Noether (23 March
¹⁸¹ 1882 – 14 April 1935) proved that every differentiable symmetry of the action - defined
¹⁸² as the integral over space of a Lagrangian density function $S = \int \mathcal{L} dt$ - of a physical
¹⁸³ system has a corresponding conservation law. More generally, a symmetry is a property
¹⁸⁴ of a physical system and under certain transformations this property is preserved.

¹⁸⁵ A gauge theory in QFT, is a theory in which the Lagrangian is invariant under a con-
¹⁸⁶ tinuous group of local transformations. Group theory was adopted to describe the sym-
¹⁸⁷ metries conserved in the SM. The gauge group of the SM is the *Lie Group* which contains
¹⁸⁸ all the transformations between possible gauges. The Lie algebra of group generators is
¹⁸⁹ associated to any Lie group and for each group generator there emerges a corresponding

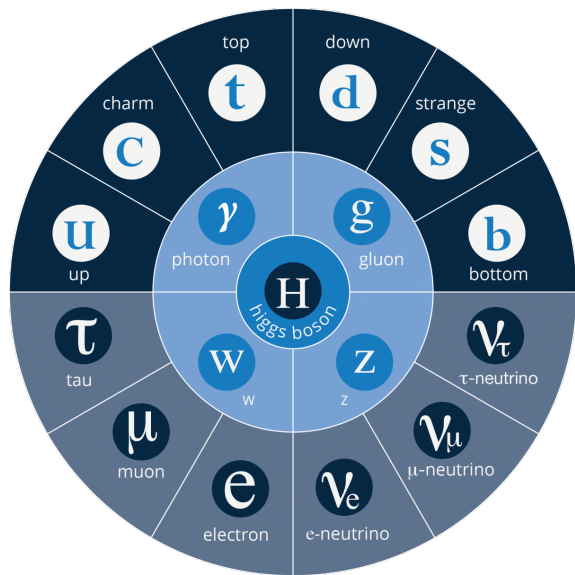


Figure 1.1: The elementary particles of the Standard Model. From the outermost to the innermost; fermions (quarks, top-half wheel, leptons, bottom-half wheel), vector bosons, and the Higgs boson.

¹⁹⁰ field, called the gauge field, and the quanta of such fields are called *gauge bosons*.

¹⁹¹ The three SM interactions can therefore be mathematically described by the following:

$$U(1)_Y \otimes SU(2)_L \otimes SU(3)_C \quad (1.1)$$

¹⁹² Here, Y is the weak hypercharge, used to estimate the correlation between the electric
¹⁹³ charge (Q) and the third component of the weak isospin (I_3) via the relation $Q = I_3 + Y/2$,
¹⁹⁴ where I_3 can either be $\pm 1/2$ or 0 for left-handed and right-handed particles, respectively;
¹⁹⁵ C the colour charge and L the left-handedness.

¹⁹⁶ QED is an Abelian gauge theory described by the symmetry group $U(1)$. The elec-
¹⁹⁷ tromagnetic four-potential is its gauge field and the photon its gauge boson [10]. The
¹⁹⁸ interactions between charged fermions occurs by the exchange of a massless photon.

¹⁹⁹ The weak interaction is described by the non-Abelian gauge group $SU(2)$. The $SU(2)$
²⁰⁰ generators are the massless gauge bosons $W_\mu^{\alpha=1,\dots,3}$ and they violate the parity by acting
²⁰¹ only on left-handed particles. As a consequence of non-Abelianity, $SU(2)$ gauge bosons
²⁰² can self-interact as the generator commutators are non-vanishing. Additionally, quarks
²⁰³ can also interact through weak interaction as mixtures of SM eigenstates as described by
²⁰⁴ the CKM matrix [11].

²⁰⁵ Finally, the strong interaction, described by the symmetry group $SU(3)$, has eight
²⁰⁶ massless gauge bosons, the gluons, $G_\mu^{\alpha=1,\dots,8}$ which can be exchanged between quarks
²⁰⁷ and can also self-interact.

²⁰⁸ Fermions

²⁰⁹ There are twelve fermions in the SM: six quarks and six leptons. In particular, fermions
²¹⁰ can be grouped into three generations. Each generation contains four particles; one up-
²¹¹ and one down-type quark, one charged lepton and one neutral lepton. The masses of the
²¹² charged leptons and quarks increase with the generation. The six quarks of the SM can
²¹³ be grouped into three $S(2)$ doublets;

$$\begin{pmatrix} u \\ d \end{pmatrix}, \quad \begin{pmatrix} c \\ s \end{pmatrix}, \quad \begin{pmatrix} t \\ b \end{pmatrix}$$

²¹⁴ The up-type quarks (*up, charm, top*) have charge $+\frac{2}{3}e$ and the down-type quarks (*down,*
²¹⁵ *strange, beauty/bottom*) have charge $-\frac{1}{3}e$, where e is the electron charge. Quarks also have
²¹⁶ another quantum number that can be seen as the analogue of the electric charge; the col-
²¹⁷ our charge. This can exist in three different states; *red, green* and *blue*, but they cannot

²¹⁸ exist as free particles. They rather group to form hadronic matter, also known as *hadrons*.
²¹⁹ There are two kinds of hadrons; mesons and baryons. Mesons are quark-antiquark
²²⁰ systems, e.g. the pion, and baryons are three-quark system, e.g. protons and neutrons.
²²¹ Quarks and anti-quarks have a baryon number of $\frac{1}{3}$ and $-\frac{1}{3}$, respectively.

²²² There are six leptons and they can be classified in charged leptons (electron e , muon
²²³ μ , tau τ) and neutral leptons (electron neutrino ν_e , muon neutrino ν_μ , tau neutrino ν_τ).

$$\begin{pmatrix} \nu_e \\ e^- \end{pmatrix}, \quad \begin{pmatrix} \nu_\mu \\ \mu^- \end{pmatrix}, \quad \begin{pmatrix} \nu_\tau \\ \tau^- \end{pmatrix}$$

²²⁴ Each lepton has a characteristic quantum number, called lepton number (L). Negat-
²²⁵ ively (positively) charged leptons have $L = -1$ ($L = 1$) and neutral leptons have $L = 1$.
²²⁶ The lepton number is conserved in all the interactions.

²²⁷ Forces of Nature

²²⁸ Forces in the SM are described by gauge theories, where the interactions are mediated by
²²⁹ a vector gauge boson.

²³⁰ The electromagnetic force is described by Quantum Electrodynamics (QED) and, as
²³¹ its mediator is the photon (γ) which couples to charged particles, it only affects charged
²³² leptons and quarks, not neutrinos which are instead affected by the weak force, mediated
²³³ by the W^\pm and Z^0 bosons.

²³⁴ The weak interaction is associated with handedness (the projection of a particle spin
²³⁵ onto its direction of motion). Both leptons and quarks have left- and right-handed com-
²³⁶ ponents. However, only the left-handed (right-handed) component for neutrinos (anti-
²³⁷ neutrinos) has been observed. This means that nature prefers to produce left-handed
²³⁸ neutrinos and right-handed anti-neutrinos, which is the so-called *parity violation*.

²³⁹ The strong interaction, mediated by the gluon, electrically neutral and massless, is de-
²⁴⁰ scribed by Quantum Chromodynamics (QCD). Its coupling (α_s) increases with increas-
²⁴¹ ing distance and is smaller at short range. In particular, α_s evolves as a function of the
²⁴² transferred four-momentum squared, Q^2 , as follows:

$$\alpha_s(Q^2) \propto \frac{1}{n_f \log\left(\frac{Q^2}{\Lambda_{\text{QCD}}^2}\right)} \quad (1.2)$$

²⁴³ where n_f is the number of quarks with mass below Q^2 and Λ_{QCD} is the QCD characteristic
²⁴⁴ scale, so Eq. 1.2 shows that α_s decreases as a function of Λ_{QCD} , but at the same time it

²⁴⁵ quickly diverges when Q^2 gets closer to Λ . In other words, as the condition $\alpha_s \ell^+ \ell^- 1$ only
²⁴⁶ holds for $Q^2 \gg \Lambda_{\text{QCD}}$, QCD can be treated perturbatively only at high energy scales.

²⁴⁷ Moreover, three facts arise;

- ²⁴⁸ • *confinement*: quarks or gluons cannot be observed as free particles, but only colourless “singlet” states can be observed as “jets”, namely collimated cone-shaped sprays of hadrons;
- ²⁵¹ • *asymptotic freedom*: interactions between quarks and gluons become weaker as the energy scale increases and the corresponding length scale decreases, as $\alpha_s \rightarrow 0$ for $Q^2 \rightarrow \infty$;
- ²⁵⁴ • *hadronisation*: when quarks or gluons are pulled apart, the production of pairs of hadrons, produced from the vacuum, is energetically preferred to an increase in distance.

²⁵⁷ Table 1.1 summarises the forces described in the SM and the main characteristics of
²⁵⁸ the mediators. The gravitational force is believed to be mediated by the graviton, but as
²⁵⁹ already mentioned, since it is not included in the SM, it will not be further discussed.

Table 1.1: Forces and mediators described by the SM

Force	Name	Symbol	Mass [GeV]	Charge
Electromagnetic	Photon	γ	0	0
Weak	W	W^\pm	80.398	$\pm e$
	Z	Z^0	91.188	0
Strong	Gluon	g	0	0

²⁶⁰ 1.1.1 Electroweak Symmetry Breaking and the Higgs mechanism

²⁶¹ In 1979 Sheldon Glashow, Abdus Salam, and Steven Weinberg were awarded the Nobel
²⁶² Prize in Physics for their contributions to the so-called electroweak unification. In the
²⁶³ mathematical description of the SM in 1.1, the electroweak interaction is described by
²⁶⁴ $U(1)_Y \otimes SU(2)_L$.

²⁶⁵ The four electroweak physical bosons W^\pm , Z and γ are related to the four unphysical
²⁶⁶ gauge bosons $W_\mu^{\alpha=1,\dots,3}$ and B_μ . In particular, to obtain the physical bosons the gauge

²⁶⁷ bosons have to mix as follows;

$$A_\mu = W_\mu^3 \sin \theta_W + B_\mu \cos \theta_W \quad (1.3)$$

²⁶⁸

$$Z_\mu = W_\mu^3 \cos \theta_W - B_\mu \sin \theta_W \quad (1.4)$$

²⁶⁹

$$W_\mu^\pm = \frac{1}{\sqrt{2}} (W_\mu^1 \mp i W_\mu^2) \quad (1.5)$$

²⁷⁰ Here, θ_W is the so-called *Weinberg angle* which is the angle by which spontaneous symmetry breaking rotates the original gauge bosons W_μ^3 and B_μ into the physical Z and γ .
²⁷¹ A_μ and Z_μ are the photon and the Z boson fields, respectively. The θ_W angle can be ex-
²⁷² perimentally determined in terms of the coupling strengths, of the $B_\mu(g_1)$ and the $W_\mu^\alpha(g_2)$
²⁷³ to the fermions, using the relation $\tan \theta_W = g_1/g_2$. The field mixing of gauge bosons that
²⁷⁴ gives birth to the physical ones can be mathematically expressed by the following:

²⁷⁶ The mass terms for both gauge bosons and fermionic fields are forbidden by the elec-
²⁷⁷ troweak gauge as they are not invariant under gauge transformations. Nonetheless, it was
²⁷⁸ experimentally proven that W and Z bosons are massive [10], therefore in order for the
²⁷⁹ SM assumption to hold, the electroweak symmetry must be broken.

²⁸⁰ The SM Lagrangian can be written as the sum of the various Lagrangians describing
²⁸¹ the three interactions and the masses of the elementary particles as follows:

$$\mathcal{L}_{\text{SM}} = \mathcal{L}_{\text{EWK}} + \mathcal{L}_{\text{QCD}} + \mathcal{L}_{\text{Mass}} \quad (1.6)$$

²⁸² In order for the SM Lagrangian to remain a renormalisable theory, the mass terms ($\mathcal{L}_{\text{Mass}}$)
²⁸³ cannot be inserted by hand. A mechanism, that can preserve the gauge symmetry in the
²⁸⁴ SM and can solve the inconsistency arisen from the mass difference between the gauge
²⁸⁵ bosons and the physical ones, is needed. A British theoretical physicist, Peter Higgs (29
²⁸⁶ May 1929, Newcastle upon Tyne, UK), came up with a brilliant solution for which he was
²⁸⁷ awarded the Nobel Prize in Physics in 2013. Higgs proposed that broken symmetry in
²⁸⁸ the electroweak theory could explain the origin of masses of elementary particles, and in
²⁸⁹ particular of W and Z bosons. The mechanism introduces a scalar field, known as the
²⁹⁰ Higgs field, thought to couple to both massive fermions and bosons. The $SU(2)$ doublet
²⁹¹ is then introduced in the SM;

$$\phi = \begin{pmatrix} \phi^+ \\ \phi^0 \end{pmatrix} \quad (1.7)$$

²⁹² with ϕ^+ and ϕ^0 generic complex fields:

$$\phi^+ = \frac{\phi_1 + i\phi_2}{\sqrt{2}}, \quad \phi^0 = \frac{\phi_3 + i\phi_4}{\sqrt{2}} \quad (1.8)$$

²⁹³ Consider a Lagrangian of the form:

$$\mathcal{L}_{\text{Higgs}} = (\partial_\mu \phi)^* (\partial^\mu \phi) - V(\phi) \quad (1.9)$$

²⁹⁴ Renormalizability and $SU(2)_L \otimes U(1)_Y$ invariance require the Higgs potential to be of the
²⁹⁵ following form:

$$V(\phi) = \mu^2 \phi^\dagger \phi + \lambda \left(\phi^\dagger \phi \right)^2 \quad (1.10)$$

²⁹⁶ The Lagrangian in Eq. 1.9 is the Higgs Lagrangian if ϕ is chosen to be the following:

$$\phi = \begin{pmatrix} \phi^+ \\ \phi^0 \end{pmatrix} = \begin{pmatrix} G^+ \\ \frac{1}{\sqrt{2}} (v + H + iG^0) \end{pmatrix}$$

²⁹⁷ Here, the complex scalar field G^\pm and the real scalar field G^0 correspond to Goldstone
²⁹⁸ bosons, and the real scalar field H is the SM Higgs boson field [12]. These massless scalars
²⁹⁹ are absorbed due to the gauge transformations by the electroweak gauge bosons of the SM:

$$\phi = \begin{pmatrix} \phi^+ \\ \phi^0 \end{pmatrix} = \begin{pmatrix} 0 \\ \frac{1}{\sqrt{2}} (v + H) \end{pmatrix} \quad (1.11)$$

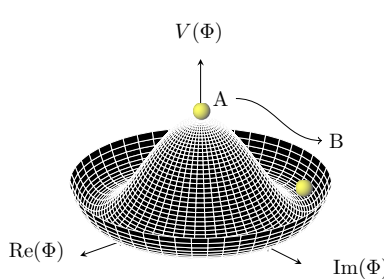
³⁰⁰

³⁰¹

³⁰²

³⁰³

³⁰⁴



The Higgs potential in Eq. 1.10 is displayed in Fig. 1.2 if λ and μ are chosen to be real. Such potential has a non-zero ground state, v , also known as *vacuum expectation value* (VEV):

$$\phi_0 = \begin{pmatrix} 0 \\ \frac{1}{\sqrt{2}} v \end{pmatrix} \quad (1.12)$$

Figure 1.2: The Higgs potential in the complex plane.

³⁰⁵ Such representation remains invariant under $U(1)$ allowing electric charge conservation.
³⁰⁶ However, the SM gauge symmetry 1.1 is broken into $SU(2)_L \otimes U(1)_Y$.

³⁰⁷ In summary, to generate particle masses gauge symmetry must be broken. However,
³⁰⁸ in order for the theory to remain renormalisable, the global Lagrangian symmetry must
³⁰⁹ be preserved. This can be solved introducing the concept of *spontaneous symmetry break-*
³¹⁰ *ing* (SSB): a mechanism that allows a symmetric Lagrangian, but not a symmetric vacuum.

311 In particular, given a Lagrangian invariant under a certain transformation, T_X , and a gen-
 312 eric set of states, that transform under T_X as the elements of a multiplet, the symmetry is
 313 spontaneously broken if one of those states is arbitrarily chosen as the ground state of the
 314 system. The interaction of the Higgs field with the $SU(2) \otimes U(1)$ gauge fields, $W_\mu^{\alpha=1,2,3}$,
 315 result in the three gauge bosons fields acquiring mass whilst the A_μ field remains mass-
 316 less.

317 1.1.2 Limitations of the Standard Model

318 During Run 1 and 2 of the LHC, the SM has been extensively validated, as shown in
 319 Fig. 1.3: the agreement, between the measured production cross-section of various SM
 320 processes and the SM predictions, looks very good. However, there are some fundamental
 321 questions that have still no answer.

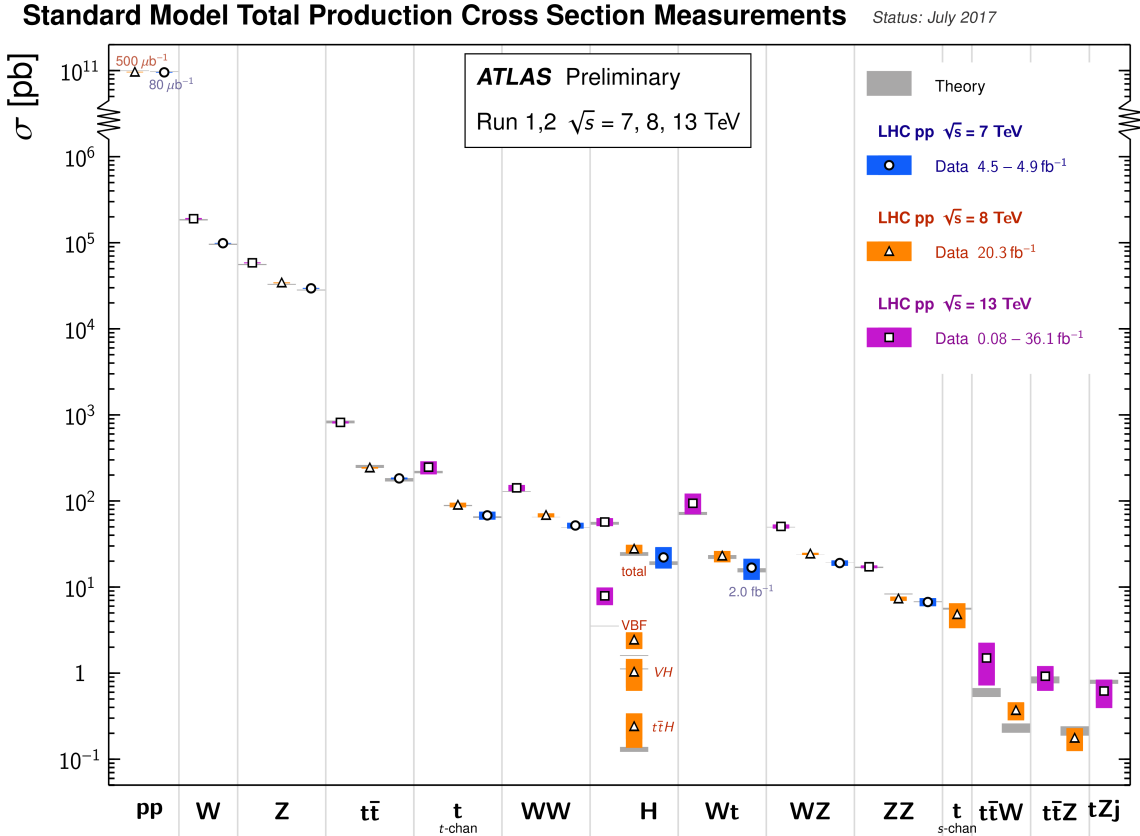


Figure 1.3: Summary of several Standard Model total production cross-section measurements, corrected for leptonic branching fractions, compared to the corresponding theoretical expectations. All theoretical expectations were calculated at NLO or higher. The luminosity used for each measurement is indicated close to the data point. Uncertainties for the theoretical predictions are quoted from the original ATLAS papers. They were not always evaluated using the same prescriptions for PDFs and scales. Not all measurements are statistically significant yet [1].

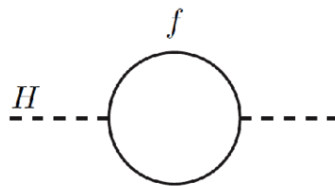


Figure 1.4: One-loop quantum corrections to the Higgs mass. A fermion correction with coupling λ_f .

322 **Hierarchy Problem**

323 Due to the coupling of the Higgs field to the fermionic fields the one-loop corrections to
324 the Higgs mass receive several contributions. In particular, looking at Fig. 1.4:

$$\Delta m_H^2 = -\frac{|\lambda_f|^2}{8\pi^2} \Lambda_{\text{UV}}^2 + \dots \quad (1.13)$$

325 where, λ_f is the coupling constant to the fermionic field; Δm_H^2 is the difference between
326 the observed Higgs mass m_H^2 and the bare mass, m_H^0 (Lagrangian parameter); Λ_{UV} is
327 the ultraviolet momentum cut-off, selected to be at the Planck scale ($\sim 2 \cdot 10^{18}$ GeV), at
328 which a QFT description of gravity is believed to become possible. The correction to the
329 Higgs mass then, will be around 30 orders of magnitude larger than Higgs mass itself,
330 in opposition to what has been measured. This difference just mentioned, between the
331 electroweak scale and the Planck scale arisen from the quantum corrections to the Higgs
332 mass, is the so-called Hierarchy Problem [13].

333 **Neutrino Masses**

334 The Super-Kamiokande Collaboration first, in 1998 [14], and SNO Collaboration later, in
335 2001 [15], have provided measurements of the neutrino flux from solar and atmospheric
336 sources. The Nobel Prize in Physics 2015 was awarded jointly to Takaaki Kajita and Arthur
337 B. McDonald “for the discovery of neutrino oscillations, which shows that neutrinos have
338 mass” [16]. Such feature contradicts the presence of the neutrinos in the SM which are
339 assumed to be massless.

340 **Dark Matter**

341 Although dark matter (DM) has never been directly observed, its existence is inferred from
342 its gravitational effects. For example, looking at galaxies rotation, it was observed that the
343 rotation speed was higher than expected, given the amount of visible matter. Two differ-
344 ent reasoning arose during the last century to justify such effect: there is either matter that

³⁴⁵ cannot be seen by us (in terms of visible light), which contributes to the galactic mass, or
³⁴⁶ the general relativity works differently at galactic distances. The former is believed to
³⁴⁷ be the most likely and it implies the existence of new particles which do not interact via
³⁴⁸ electromagnetic interaction, the so-called Weakly Interacting Massive Particles (WIMPs).

³⁴⁹ 1.2 Supersymmetry

³⁵⁰ Supersymmetry, also known as SUSY, introduces a space-time symmetry that relates bo-
³⁵¹ sons to fermions and vice-versa, via a transformation of the form of:

$$Q |\text{fermion}\rangle = |\text{boson}\rangle, \quad Q |\text{boson}\rangle = |\text{fermion}\rangle \quad (1.14)$$

³⁵² For each SM particle there exists a supersymmetric partner, generally called *sparticle* (where
³⁵³ the s stands for “scalar”), with a spin difference of $\Delta s = 1/2$. Each pair of partners is ar-
³⁵⁴ ranged in a so-called *supermultiplet*. The two components have same masses and quantum
³⁵⁵ numbers, but different spin. *Sleptons* and *squarks* gauge quantum numbers are the same
³⁵⁶ as their SM equivalent, namely for example, the superpartners of the left-handed SM fer-
³⁵⁷ mion components couple weakly, but the superpartners of the right-handed SM fermion
³⁵⁸ components do not. Furthermore, gauge supermultiplets contain a vector boson and two
³⁵⁹ spin- $\frac{1}{2}$ fermions. Spin-1 bosons are arranged in gauge multiplets, and their superpartners,
³⁶⁰ referred to as *gauginos*, are spin- $\frac{1}{2}$ fermions. Unlike the SM, the Spin-0 Higgs boson has
³⁶¹ two supermultiplets containing sparticles with different weak isospin values, referred to
³⁶² as H_u and H_d , which are required to give mass to both the up- and down-type sparticles.
³⁶³ Higgs SUSY partners are called the *Higgsinos*.

³⁶⁴ As of today, SUSY particles have not been observed, resulting in the assumption that
³⁶⁵ SUSY must be a broken symmetry, otherwise superpartners would have the same masses
³⁶⁶ as their SM equivalent. However, if sparticles were to be too heavy (close to the Planck
³⁶⁷ scale), the hierarchy problem would still remain unsolved. The *soft* SUSY breaking mech-
³⁶⁸ anism, described in Section 1.2.2, overcomes this problem by imposing constraints on the
³⁶⁹ masses of sparticles to a range that can be experimentally explored.

³⁷⁰ 1.2.1 Why SUSY?

³⁷¹ One of the main motivations for SUSY is the cancellation of quadratic divergences to
³⁷² Δm_H^2 . The introduction of SUSY particles, with a half-integer spin difference with re-
³⁷³ spect to their SM partners, provides a solution to the hierarchy problem. The Higgs mass

³⁷⁴ squared potential receives corrections from a new scalar of mass of the form:

$$\Delta m_H^2 = -\frac{|\lambda_S|^2}{16\pi^2} \left[\Lambda_{UV}^2 - 2m_S^2 \ln(\Lambda_{UV}/m_S) + \dots \right] \quad (1.15)$$

³⁷⁵ where, λ_S is the coupling of SUSY particles to the Higgs field. This term cancels the
³⁷⁶ fermionic contributions in Eq. 1.13 since the couplings are the same. The experimental
³⁷⁷ value of Higgs mass will then not need any fine tuning.

³⁷⁸ Furthermore, Fig. 1.5 shows the inverse couplings as a function of the scale for both SM
³⁷⁹ and the Minimal Supersymmetric Standard Model (MSSM), which will be soon discussed.
³⁸⁰ In the SM the three lines, representing electromagnetic (dashed blue), weak (dashed red)
³⁸¹ and strong (solid green) interactions respectively, do not meet at one point, but with the
³⁸² introduction of supersymmetry, and assuming that the supersymmetric particles are not
³⁸³ heavier than about 1 TeV, they do meet. This is an indication that supersymmetry could
³⁸⁴ be discovered at the LHC as well as another good motivation for SUSY searches given the
³⁸⁵ possible unification of the coupling constants at the Planck scale.

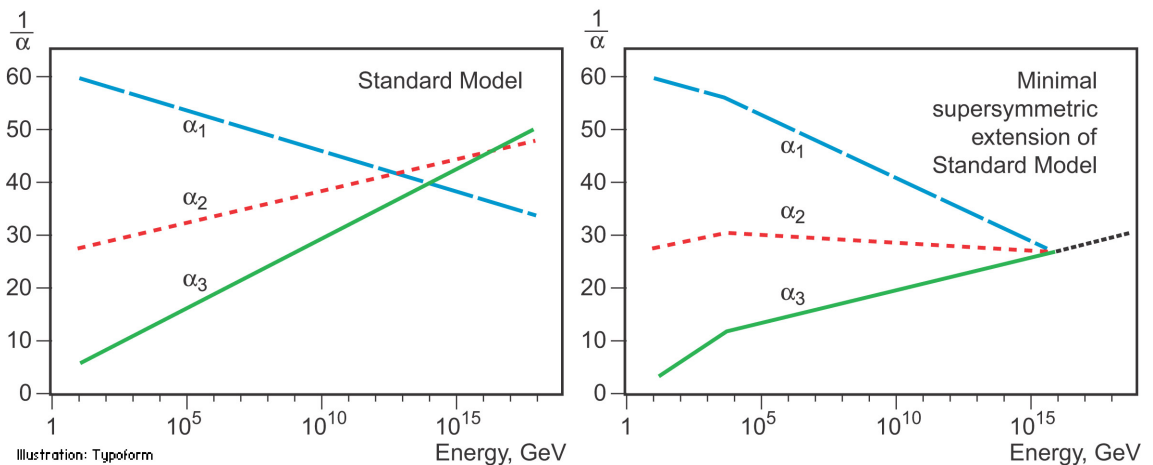


Figure 1.5: The inverse couplings of electromagnetic (dashed blue), weak (dashed red) and strong (solid green) interactions with the SM (left) and a supersymmetric model (right). In the SM the three lines do not meet at one point, but with the introduction of supersymmetry, and assuming that the supersymmetric particles are not heavier than about 1 TeV, they do meet. This is an indication that supersymmetry could be discovered at the LHC.

³⁸⁶ 1.2.2 Minimal Supersymmetric Standard Model

³⁸⁷ There does not exist a unique extension of a supersymmetric Standard Model, i. e. SUSY
³⁸⁸ is not a well-defined model but it is more a framework within which various SM exten-
³⁸⁹ sions can be derived. The Minimal Supersymmetric Standard Model (MSSM), a minimal
³⁹⁰ supersymmetric extension of the SM [17], is defined by essentially doubling up the num-

³⁹¹ ber of particles in the SM theory in order to include all the SM particles as well as their
³⁹² corresponding superpartners.

³⁹³ Soft SUSY breaking

³⁹⁴ The mass spectrum of the SUSY particles must sit somewhere at a larger scale than the SM
³⁹⁵ one, as supersymmetric particles have not been discovered at the mass scale of their SM
³⁹⁶ partners. This gives us a hint that supersymmetry cannot be an exact symmetry, there has
³⁹⁷ to be an analogy with the electroweak symmetry breaking discussed in 1.1.1 that breaks
³⁹⁸ SUSY. In particular, this must be soft or spontaneous such that broken supersymmetry
³⁹⁹ still provides a solution to the hierarchy problem. This means that some new higher-
⁴⁰⁰ energy-scale particles and interactions have to be added to the MSSM, but it also means
⁴⁰¹ that terms, containing only masses and couplings, with positive mass dimension, gauge
⁴⁰² invariant and violating SUSY, have to be added to the Lagrangian;

$$\mathcal{L}_{\text{MSSM}} = \mathcal{L}_{\text{SUSY}} + \mathcal{L}_{\text{soft}} \quad (1.16)$$

⁴⁰³ Here, $\mathcal{L}_{\text{SUSY}}$ contains the original SUSY invariant interaction and $\mathcal{L}_{\text{soft}}$ contains all the
⁴⁰⁴ additional terms. A set of around 100 parameters - depending on the method - are then
⁴⁰⁵ introduced into the theory.

⁴⁰⁶ A large amount of theoretical effort has been spent trying to understand the mech-
⁴⁰⁷anism for soft SUSY breaking in order to produce the desired superpartner masses and
⁴⁰⁸ interactions properties. Among these three most studied mechanisms are;

- ⁴⁰⁹ • gravity-mediated supersymmetry breaking, also known as mSUGRA (minimal su-
⁴¹⁰pergravity), which communicates supersymmetry breaking to the supersymmetric
⁴¹¹Standard Model through gravitational interactions [18];
- ⁴¹² • gauge-mediated supersymmetry breaking (GMSB) which communicates supersym-
⁴¹³metry breaking to the supersymmetric Standard Model through the Standard Model's
⁴¹⁴gauge interactions [19];
- ⁴¹⁵ • anomaly-mediated supersymmetry breaking (AMSB), a special type of gravity-mediated
⁴¹⁶supersymmetry breaking, that communicates supersymmetry breaking to the su-
⁴¹⁷persymmetric Standard Model through the conformal anomaly [20, 21]

418 MSSM mass spectrum

419 As per the SM gauge bosons, the gaugino masses are affected by electroweak symmetry
 420 breaking. The new states, introduced in the $\mathcal{L}_{\text{soft}}$, mix to form the mass eigenstates of
 421 the sparticles. The neutral Winos, \tilde{W}^0 , Binos, \tilde{B}^0 and higgsinos \tilde{H}^0 mix to form the four
 422 *neutralinos* $\tilde{\chi}_i^0$ ($i = 1, 2, 3, 4$) as follows;

$$\begin{pmatrix} \tilde{\chi}_1^0 \\ \tilde{\chi}_2^0 \\ \tilde{\chi}_3^0 \\ \tilde{\chi}_4^0 \end{pmatrix} = \begin{pmatrix} M_1 & 0 & -c_\beta s_W m_Z & c_W s_\beta m_Z \\ 0 & M_2 & c_\beta c_W m_Z & -c_W s_\beta m_Z \\ -c_\beta s_W m_Z & c_\beta s_W m_Z & 0 & -\mu \\ s_\beta c_W m_Z & -s_\beta c_W m_Z & -\mu & 0 \end{pmatrix} \begin{pmatrix} \tilde{B}^0 \\ \tilde{W}^0 \\ \tilde{H}_u^0 \\ \tilde{H}_d^0 \end{pmatrix} \quad (1.17)$$

423 Here, $c_\beta = \cos \beta$, $(s_\beta) = \sin \beta$, $c_W = \cos \theta_W$ and $(s_W) = \sin \theta_W$. M_1, M_2 are related to
 424 gaugino masses and μ to higgsino mass, $\tan \beta$ is the ratio of the VEVs of the two Higgs
 425 doublet fields, θ_W is the ratio of the electroweak coupling constants and, m_Z (m_W) is the
 426 mass of the Z (W) boson. The neutralino indeces are conventionally assumed to increase
 427 with their masses. The charged winos \tilde{W}^\pm and higgsinos \tilde{H}^\pm mix to form four *charginos*,
 428 $\tilde{\chi}_i^\pm$ ($i = 1, 2$) as it follows;

$$\begin{pmatrix} \tilde{\chi}_1^\pm \\ \tilde{\chi}_2^\pm \end{pmatrix} = \begin{pmatrix} M_2 & \sqrt{2}m_W s_\beta \\ \sqrt{2}m_W c_\beta & \mu \end{pmatrix} \begin{pmatrix} \tilde{W}^\pm \\ \tilde{H}^\pm \end{pmatrix} \quad (1.18)$$

429 Charginos and neutralinos mix as described in Eq. 1.18 and 1.17 and will be referred
 430 to as bino-like, wino-like or higgsino-like depending on their phenomenology. Gluinos
 431 do not mix as they carry colour charge.

432 The Higgs sector is also affected. There are five mass eigenstates, h^0, H^0, A^0 , and H^\pm .
 433 These, together with the other MSSM particles are listed in Table 1.2.

434 In the MSSM the squark sector is specified by the mass matrix in the basis $(\tilde{q}_L, \tilde{q}_R)$ with
 435 $\tilde{q} = \tilde{t}$ or \tilde{b} [22]. A rotation matrix can be defined also for left- and right-handed squarks
 436 and sleptons, although in the MSSM the mixing is assumed to be non-zero only for the
 437 third-generation scalar partners. Stop, \tilde{t}_L, \tilde{t}_R , sbottom \tilde{b}_L, \tilde{b}_R , and stau, $\tilde{\tau}_L, \tilde{\tau}_R$ rotate into
 438 mass eigenstates, $\tilde{t}_1, \tilde{t}_2, \tilde{b}_1, \tilde{b}_2, \tilde{\tau}_1, \tilde{\tau}_2$, respectively, as described in Eq. 1.19 [23].

$$\mathcal{M}_{\tilde{q}}^2 = \begin{pmatrix} m_{\tilde{q}_L}^2 & a_q m_q \\ a_q m_q & m_{\tilde{q}_R}^2 \end{pmatrix} \quad (1.19)$$

439 with

Table 1.2: SUSY particles in the MSSM

Name	Spin	Gauge Eigenstates	Mass Eigenstates
Squarks (\tilde{q})	0	$\tilde{u}_L \tilde{u}_R \tilde{d}_L \tilde{d}_R$	(same)
		$\tilde{c}_L \tilde{c}_R \tilde{s}_L \tilde{s}_R$	(same)
		$\tilde{t}_L \tilde{t}_R \tilde{b}_L \tilde{b}_R$	$\tilde{t}_1 \tilde{t}_2 \tilde{b}_1 \tilde{b}_2$
Sleptons (\tilde{l})	0	$\tilde{e}_L \tilde{e}_R \tilde{\nu}_L$	(same)
		$\tilde{\mu}_L \tilde{\mu}_R \tilde{\nu}_L$	(same)
		$\tilde{\tau}_L \tilde{\tau}_R \tilde{\nu}_{\tau}$	$\tilde{\tau}_1 \tilde{\tau}_2 \tilde{\nu}_{\tau}$
Higgs bosons	0	$H_u^0 H_d^0 H_u^+ H_d^-$	$h^0 H^0 A^0 H^{\pm}$
Neutralinos ($\tilde{\chi}_j^0$)	1/2	$\tilde{B}^0 \tilde{W}^0 \tilde{H}_u^0 \tilde{H}_d^0$	$\tilde{\chi}_1^0 \tilde{\chi}_2^0 \tilde{\chi}_3^0 \tilde{\chi}_4^0$
Charginos ($\tilde{\chi}_i^{\pm}$)	1/2	$\tilde{W}^{\pm} \tilde{H}_u^{\pm} \tilde{H}_d^{\mp}$	$\tilde{\chi}_1^{\pm} \tilde{\chi}_2^{\pm}$
Gluino	1/2	\tilde{g}	(same)
Gravitino	3/2	\tilde{G}	(same)

$$\begin{aligned}
m_{\tilde{q}_L}^2 &= M_{\tilde{Q}}^2 + m_Z^2 \cos 2\beta \left(I_3^{q_L} - e_q \sin^2 \theta_W \right) + m_q^2, \\
m_{\tilde{q}_R}^2 &= M_{\{\tilde{U}, \tilde{D}\}}^2 + m_Z^2 \cos 2\beta e_q \sin^2 \theta_W + m_q^2, \\
a_q m_q &= \begin{cases} (A_t - \mu \cot \beta) m_t, (\tilde{q} = \tilde{t}) \\ (A_b - \mu \tan \beta) m_t, (\tilde{q} = \tilde{b}) \end{cases}
\end{aligned} \tag{1.20}$$

Here, $I_3^{q_L}$ is the third component of the weak isospin and e_q the electric charge of the quark q . $M_{\{\tilde{Q}, \tilde{U}, \tilde{D}\}}$ and $A_{t,b}$ are soft SUSY-breaking parameters, μ is the higgsino mass parameter, and $\tan \beta$, as previously mentioned, is the ratio of Higgs field VEVs. By diagonalising the matrix in Eq. 1.19 one gets the mass eigenstates

$$\tilde{q}_1 = \tilde{q}_L \cos \theta_{\tilde{q}} + \tilde{q}_R \sin \theta_{\tilde{q}}$$

$$\tilde{q}_2 = -\tilde{q}_L \sin \theta_{\tilde{q}} + \tilde{q}_R \cos \theta_{\tilde{q}}$$

with the mass eigenvalues $m_{\tilde{q}_1}, m_{\tilde{q}_2}$ ($m_{\tilde{q}_1} < m_{\tilde{q}_2}$) and the mixing angle $\theta_{\tilde{q}}$ ($-\pi/2 < \theta_{\tilde{q}} \leq \pi/2$).

1.2.3 Phenomenology of Supersymmetry

As previously mentioned, the introduction of SUSY particles overcomes the problem of an unnatural fine-tuning to the Higgs mass due to its quadratic corrections.

448 *R-parity*

449 The most general MSSM can contain operators that violate baryon and/or lepton number,
450 thus allowing proton decays. The non-observation of proton decays forbids the existence
451 of such terms. A possibility to avoid these operators is to introduce a new discrete sym-
452 metry named *R-parity*. The conserved quantum number is defined as;

$$P_R = (-1)^{3(B-L)+2s} \quad (1.21)$$

453 where B , L , and s are the baryon, lepton, and spin number, respectively.

454 The SM particles have $R = 1$ and SUSY partners have $R = -1$. When *R-parity* conser-
455 vation is imposed on MSSM models, the mixing between particles and sparticles cannot
456 occur, resulting in the number of SUSY particles to be even at every interaction vertex. Fur-
457 thermore, all sparticles must be pair-produced and the Lightest Supersymmetric Particle
458 (LSP) has to be stable and can be a good Dark Matter candidate.

459 Although SUSY searches in a *R-parity* violating (RPV) scenario have been extensively
460 investigated by the particle-physics community, in this work only *R-parity* conserving
461 (RPC) models, where the $\tilde{\chi}_1^0$ is assumed to be the LSP, were considered.

462 **Phenomenological MSSM (pMSSM)**

463 As mentioned in 1.2.2, once the SUSY soft breaking occurred, the unconstrained MSSM
464 has more than 100 parameters in addition to the Standard Model ones. However, this
465 makes the SUSY searches, e.g. finding regions, in parameter space, that are consistent
466 with the data, rather impractical. Under the following three assumptions;

- 467** • no new source of CP-violation (CKM matrix is the only source)
- 468** • no Flavour Changing Neutral Currents
- 469** • first- and second-generation universality

470 the number of free parameters can be reduced down to 19. The introduction of such para-
471 meters, summarised in Table 1.3, defines the so-called phenomenological MSSM (pMSSM).
472 Such parameter space is still rather large and it makes pMSSM searches extremely chal-
473 lenging and difficult to exclude. To overcome this problem *simplified models* are introduced.
474 In other words, a certain signal process is extracted from the model and only particles
475 contributing to a certain decay mode will be considered, e.g. $\tilde{t}_1 \rightarrow t + \tilde{\chi}_1^0$ only targets the
476 2-body decay ignoring the remaining SUSY mass spectrum. The number of parameters

Table 1.3: Parameters in the pMSSM.

Parameter	Description	N. of parameters
M_1, M_2, M_3	Bino, Wino and gluino masses	3
M_A	pseudoscalar Higgs boson mass	1
μ	higgsino mass	1
$m_{\tilde{q}}, m_{\tilde{u}_R}, m_{\tilde{d}_R}$, $m_{\tilde{Q}_L}, m_{\tilde{t}}, m_{\tilde{b}}$	first- and second-generation squark masses third generation squark masses	3 3
$m_{\tilde{l}}, m_{\tilde{e}_R}$ $m_{\tilde{L}}, m_{\tilde{\tau}_R}$	first- and second-generation slepton masses third-generation slepton masses	2 2
A_t, A_b, A_τ	third-generation trilinear couplings	3
$\tan \beta$	two-higgs-doublet fields VEVs ratio	1

⁴⁷⁷ will then boil down to 2; $m_{\tilde{t}}$ and $m_{\tilde{\chi}^0}$, allowing the reinterpretation of the results and
⁴⁷⁸ providing a powerful tool to constrain various models.

⁴⁷⁹ In this work only analyses based on such simplified models will be presented.

⁴⁸⁰ Phenomenology of the top squark

⁴⁸¹ Fig. 1.6 shows SUSY particles production cross-sections in pp collisions at $\sqrt{s} = 13$ TeV for
⁴⁸² squarks that do not contribute to gluino production diagrams and vice versa, i. e. treat-
⁴⁸³ ing squarks and gluinos as *decoupled* making the cross-section of squark pair-production
⁴⁸⁴ be the same for all families. While gluino pair-production cross-sections are fairly large,
⁴⁸⁵ SUSY electroweak production cross-sections of neutralinos and charginos are consider-
⁴⁸⁶ ably lower. Slepton production cross-section, which is not displayed, would sit just below
⁴⁸⁷ higgsino-like chargino/neutralino production cross-section.

⁴⁸⁸ There exists various decay modes of pair-produced stops, depending on the masses
⁴⁸⁹ of the decay products;

- ⁴⁹⁰ • $\tilde{t} \rightarrow t \tilde{\chi}_1^0$
- ⁴⁹¹ • $\tilde{t} \rightarrow b \tilde{\chi}_1^\pm \rightarrow b W \tilde{\chi}_1^0$ (on/off-shell W) or $\tilde{t} \rightarrow b W \tilde{\chi}_1^0$ (off-shell top)
- ⁴⁹² • $\tilde{t} \rightarrow c \tilde{\chi}_1^0$
- ⁴⁹³ • $\tilde{t} \rightarrow b f f' \tilde{\chi}_1^0$

⁴⁹⁴ Figure 1.7 shows a schematic representation of the parameter space ($m_{\tilde{t}_1}, m_{\tilde{\chi}_1^0}$) and the
⁴⁹⁵ different region where each of the above-mentioned process dominates.

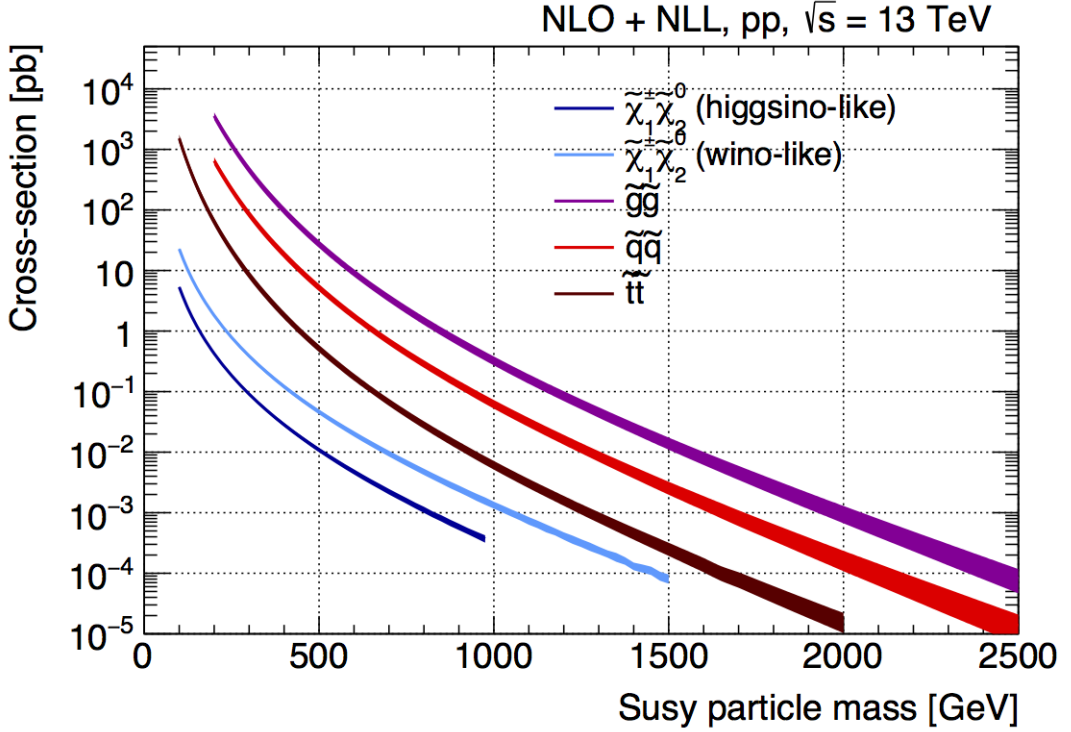


Figure 1.6: NLO+NLL production cross-sections as a function of mass at $\sqrt{s} = 13$ TeV [2]

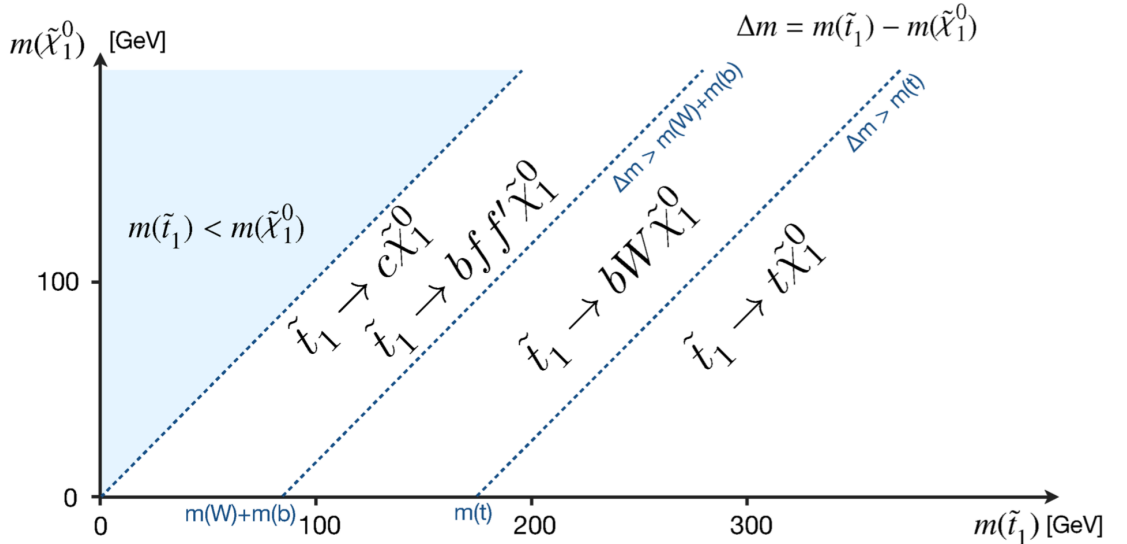


Figure 1.7: Illustration of stop decay modes in the $(m_{\tilde{t}_1}, m_{\tilde{\chi}_1^0})$ mass plane where the $\tilde{\chi}_1^0$ is assumed to be the lightest supersymmetric particle. The dashed blue lines indicate thresholds separating regions where different processes dominate.

In the models considered in this work, either $\tilde{\chi}_2^0$ or $\tilde{\chi}_1^\pm$ is assumed to be the so-called next lightest supersymmetric particle (NLSP). Three different decay scenarios were considered in this work; (a) where both top squarks decay via $\tilde{t} \rightarrow t^{(*)} \tilde{\chi}_1^0$ ¹; (b) at least one

¹ The symbol (*) indicates that the decay can occur with the top quark being produced off-shell (region

of the stops decays via $\tilde{t} \rightarrow b \tilde{\chi}_1^\pm \rightarrow b W^{(*)} \tilde{\chi}_1^0$; (c) where $m_{\tilde{\chi}_2^0}$ is small enough to allow one stop to decay via $\tilde{t} \rightarrow t \tilde{\chi}_2^0 \rightarrow h/Z \tilde{\chi}_1^0$. Here, h is the SM Higgs boson (125 GeV), as illustrated in Figure 1.8(a)–(c), respectively. Furthermore, top squarks can also be indirectly produced through the so-called gluino-mediated stop production, as shown in Figure 1.8(d).

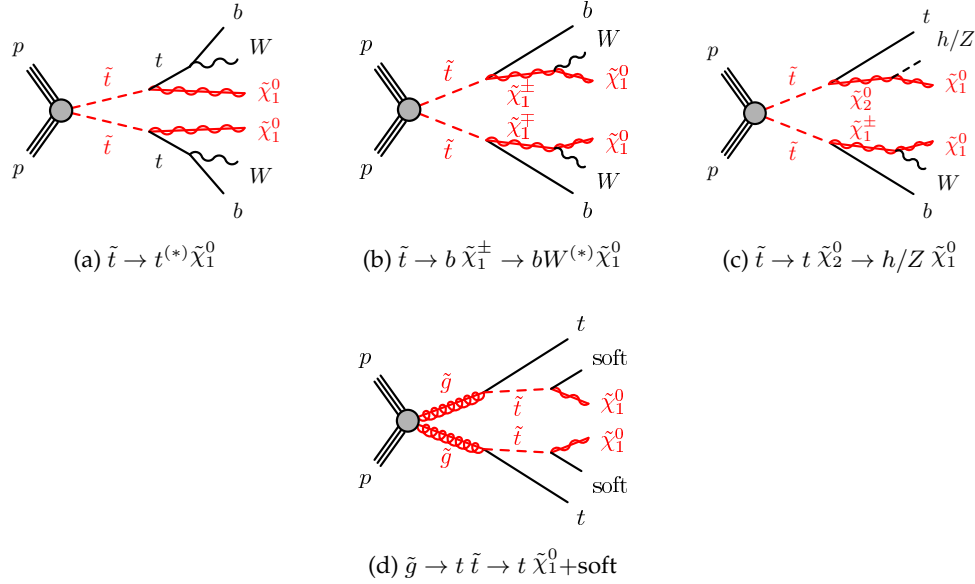


Figure 1.8: Diagrams of the decay topologies of the signal models considered in this work. The term “soft” refers to decay products that have transverse momenta below the detector thresholds.

Third-generation SUSY analyses, e. g. stop pair-production ($\tilde{t}\tilde{t}$) or sbottom pair-production ($\tilde{b}\tilde{b}$) are very challenging, due to the cross-section being around a factor of six smaller than $t\bar{t}$ production (when $m_{\tilde{t}_1} \sim m_{at}$), which usually is one of the main backgrounds. Furthermore, the cross-section of such processes dramatically decreases with increasing $m_{\tilde{q}}$. Nonetheless, for example, searches for direct \tilde{t}_1 production with $\tilde{t}_1 \rightarrow t + \tilde{\chi}_1^0$ are sensitive in a scenario where $m_{\tilde{t}_1} \gg m_t + m_{\tilde{\chi}_1^0}$ as the large E_T^{miss} , from the neutralinos, provides discriminating power for $t\bar{t}$ rejection.

between the second and third dashed line in Fig. 1.7)

511 2 | The ATLAS Experiment at the 512 LHC

513

*We are rather like children, who
must take a watch to pieces to see
how it works*

Sir Ernest Rutherford

514 ATLAS (A Toroidal LHC ApparatuS) is one of the four main experiments (ATLAS,
515 CMS, ALICE, LHCb) taking data at a center-of-mass energy of 13 TeV using beams de-
516 livered by the Large Hadron Collider (LHC). In this chapter an overview of the LHC will
517 be given in Section 2.1, then the ATLAS detector will be described in Section 2.2, and fi-
518 nally the Trigger system, used to cleverly store the data, will be described in Section 2.3. A
519 more in-depth description of the Trigger algorithms I have been involved in will be given
520 in Chapter 3.

521 2.1 The LHC

522 As of today, the LHC is the world's largest and most powerful particle accelerator. It was
523 designed to help answer some of the fundamental open questions in particle physics by
524 colliding protons at an unprecedented energy and luminosity. It is located at the European
525 Organisation for Nuclear Research (CERN), in the Geneva area, at a depth ranging from
526 50 to 175 metres underground. It consists of a 27-kilometre ring made of superconducting
527 magnets, and inside it two high-energy particle beams travel in opposite directions and
528 in separate beam pipes.

529 The beams are guided around the ring by a strong magnetic field generated by coils -
530 made of special electric cables - that can operate in a superconducting regime. 1232 super-
531 conducting dipole and 392 quadrupole magnets, with an average magnetic field of 8.3 T,

532 are employed and kept at a temperature below 1.7 K, in order to preserve their supercon-
 533 ducting properties. The formers are used to bend the beams and the latters to keep them
 534 focused while they get accelerated.

535 The collider first went live on September 2008 even though, due to a magnet quench
 536 incident that damaged over 50 superconducting magnets, it has been operational since
 537 November 2009 when low-energy beams circulated in the tunnel for the first time since the
 538 incident. This also marked the start of the main research programme and the beginning
 539 of the so-called Run 1: first operational run (2009 - 2013).

540 Performance of the LHC

541 In June 2015 the LHC restarted delivering physics data, after a two-year break, the so-
 542 called Long Shutdown 1 (LS1), during which the magnets were upgraded to handle the
 543 current required to circulate 7-TeV beams. It was the beginning of the so-called Run 2 -
 544 second operational run (2015-2018) - during which LHC has collided up to 10^{11} bunches
 545 of protons every 25 ns at the design luminosity - the highest luminosity the detector was
 546 designed to cope with - of $2 \cdot 10^{34} \text{ cm}^{-2} \text{s}^{-1}$. The definition of the luminosity is:

$$\mathcal{L} = f \frac{n_b N_1 N_2}{4\pi\sigma_x\sigma_y} \quad (2.1)$$

547 where N_1 and N_2 are the number of protons per bunch in each of the colliding beams, f
 548 is the revolution frequency of the bunch collisions, n_b the number of proton per bunch,
 549 and σ_x and σ_y are the horizontal and vertical dimensions of the beam. The luminosity is
 550 strictly related to the number of collisions occurring during a certain experiment via the
 551 following:

$$\mathcal{N}_{\text{event}} = \mathcal{L}\sigma_{\text{event}} \quad (2.2)$$

552 where σ_{event} is the cross section of the process under investigation. It has not only collided
 553 protons but also heavy ions, in particular lead nuclei at $\sqrt{s_{NN}} = 5.02 \text{ TeV}$, at a luminosity
 554 of $10^{27} \text{ cm}^{-2} \text{s}^{-1}$ [24].

555 Acceleration stages

556 Before reaching the maximum energy, the proton beams are accelerated by smaller ac-
 557 celerators through various stages. Figure 2.1 shows a sketch of the CERN's accelerator
 558 complex. It all begins at the linear accelerator LINAC 2. Here protons are accelerated up
 559 to 50 MeV, and then injected in the Proton Synchrotron Booster (PSB) where they reach

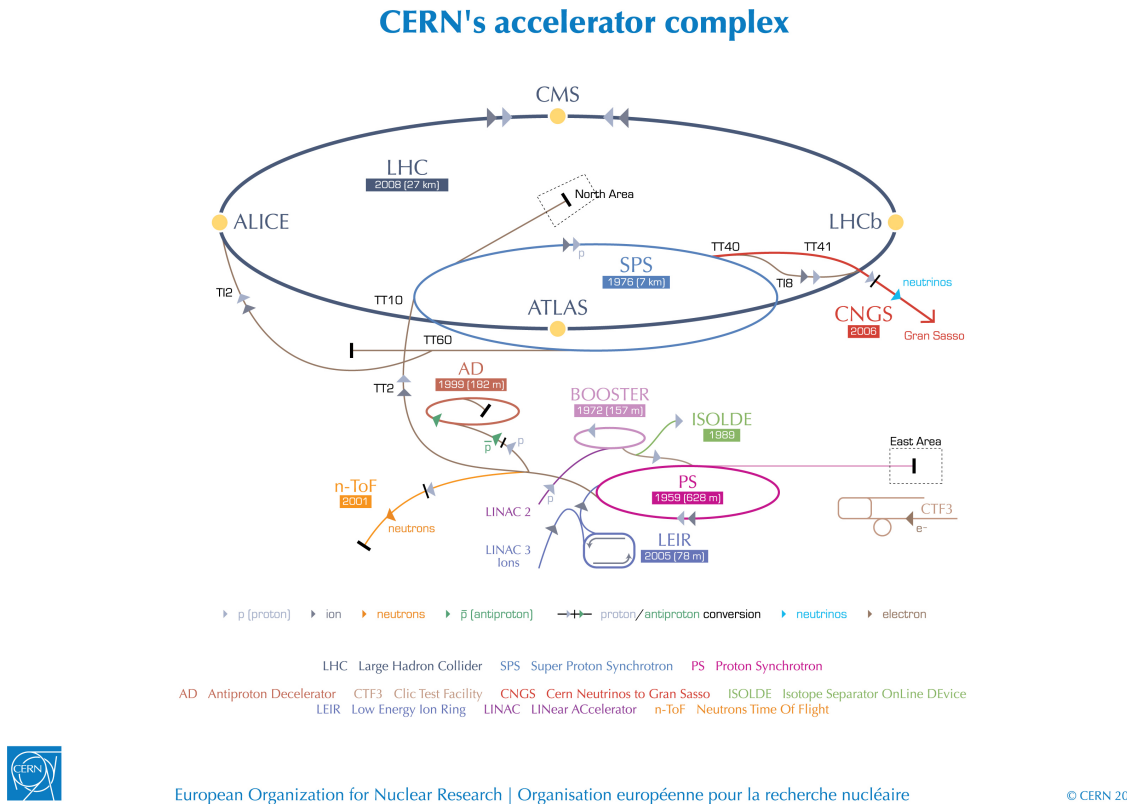


Figure 2.1: CERN Accelerator complex. The LHC is the last ring (dark grey line). Smaller machines are used for early-stage acceleration and also to provide beams for other experiments [3].

560 1.4 GeV. The next stage is the Proton Synchrotron (PS), which boosts the beams up to 25
561 GeV and then the Super Proton Synchrotron (SPS) makes them reach energies up to 450
562 GeV. Eventually, the beams are injected in bunches with a 25 ns spacing into the LHC,
563 where they travel in opposite directions, while they are accelerated to up to 13 TeV. Once
564 the bunches reach the maximum energy, they are made collide at four different points,
565 inside four experiments around the ring [25].

566 The heavy ion beams acceleration procedure is slightly different. Their journey starts
567 at LINAC 3 first, and the Low Energy Ion Ring (LEIR) then, before they make their way
568 into the PS where they follow the same path as the protons [25].

569 The four large detectors on the collision points are; the multi-purpose detectors A Tor-
570 oidal LHC ApparatuS (ATLAS), and Compact Muon Solenoid (CMS) [26], Large Hadron
571 Collider beauty (LHCb) [27], which focuses on flavour physics, and A Large Ion Collider
572 Experiment (ALICE) [28] which specialises in heavy ion physics. The *big four* are not the
573 only experiments at the CERN's accelerator complex. There also are smaller experiments
574 based at the the four caverns about the collision points e.g. TOTEM, LHCf and MoEDAL,
575 but this will not be discussed any further in this thesis.

576 2.2 The ATLAS Detector

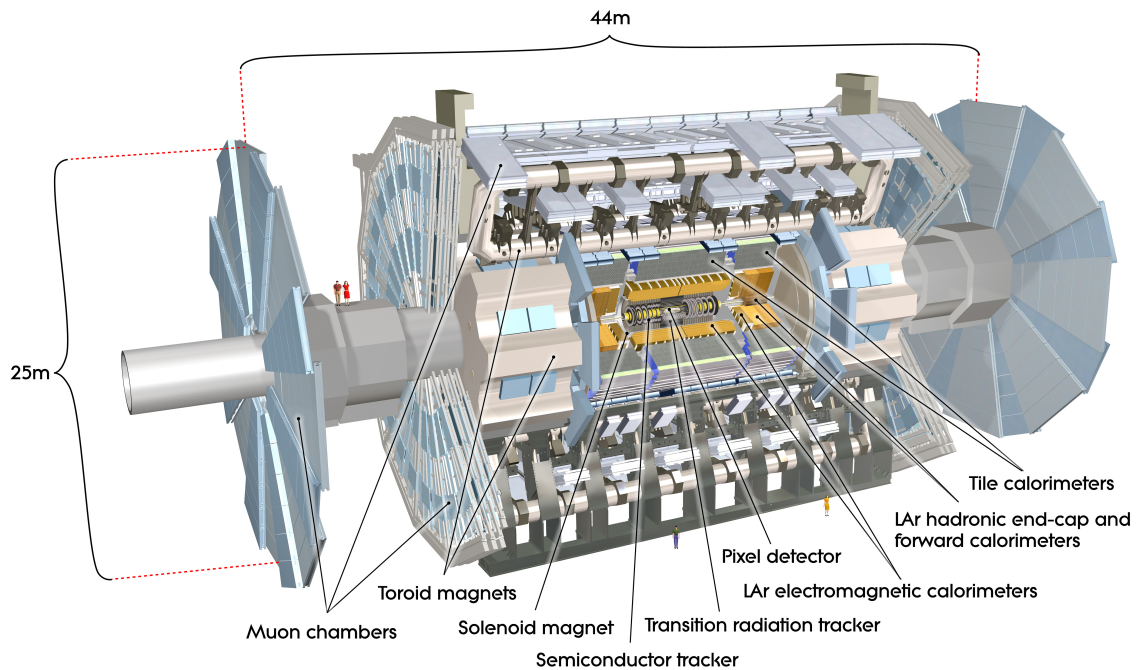


Figure 2.2: Cut-away view of the ATLAS detector. The dimensions of the detector are 25 m in height and 44 m in length. The overall weight of the detector is approximately 7000 tonnes [3].

577 ATLAS is a general-purpose detector designed to collect data with the highest luminosity provided by the LHC. It is located at CERN’s Point 1 cavern and it measures about
 578 45 m in length and 25 m in diameter. It has a forward-backward symmetric cylindrical
 579 geometry with respect to the interaction point and it is designed to reconstruct and meas-
 580 ure physics objects such as electrons, muons, photons and hadronic jets. Its design was
 581 optimised to be as sensitive as possible to the discovery of the Higgs boson and beyond-
 582 the-Standard-Model (BSM) physics. In fact, thanks to the other sub-systems, ATLAS is
 583 able to observe all possible decay products by covering nearly 4π steradians of solid angle.
 584

585 In Figure 2.2 a cut-away view of ATLAS with all its components is shown. The inner-
 586 most layer is the Inner Detector (ID) which is the core of the tracking system and consists
 587 of a Pixel, a Silicon micro-strip tracker (SCT), and a Transition Radiation Tracker (TRT).
 588 It is submerged in a 2 T magnetic field, generated by a thin superconducting solenoid,
 589 which bends all the charged particles’ trajectories allowing transverse momentum meas-
 590 urement. The electromagnetic and hadronic calorimeters form the next layer and they are
 591 both used to perform precise energy measurements of photons, electrons, and hadronic
 592 jets. Finally, the outermost layer corresponds to the Muon Spectrometer (MS) which, to-

593 gether with the ID, enclosed in a toroidal magnetic field, allows precise measurement of
 594 momentum and position of muons. These sub-detectors will be discussed in more detail
 595 in the following sections.

596 The ATLAS coordinate system

597 A coordinate system is taken on for the spatial definition of the sub-systems and kinematic
 598 measurement of physics processes. Such system is defined starting from the interaction
 599 point, defined as the origin. The z -axis is defined by the beam direction and the $x - y$
 600 plan, as transverse to the beam direction.

601 A quantity, known as pseudorapidity, (η), is defined to describe the angle of a particle
 602 coming out of the collision, with respect to the beam axis:

$$\eta \equiv -\ln(\tan(\theta/2))$$

603 Here θ is the polar angle. The azimuthal angle, ϕ , is defined around the beam axis and
 604 the polar angle. In the (η, ϕ) space a distance ΔR can be therefore defined as

$$\Delta R = \sqrt{\Delta\eta^2 + \Delta\phi^2}$$

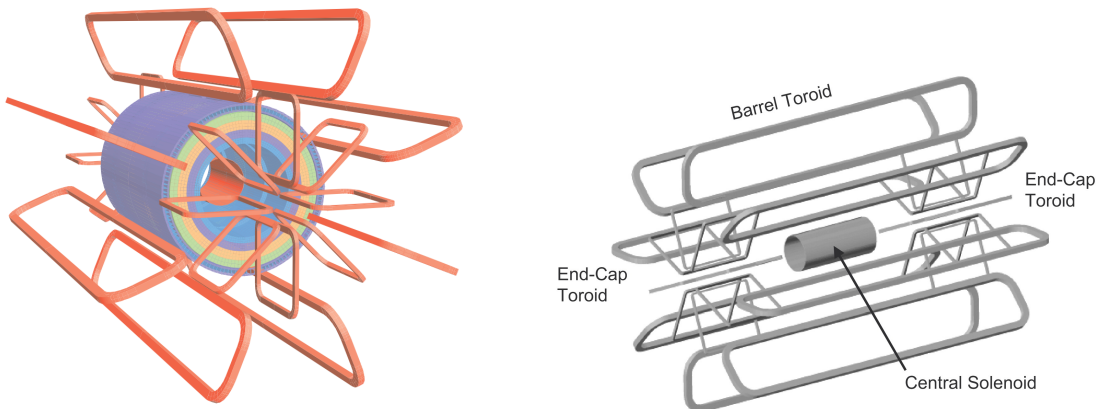
605 where $\Delta\eta$ and $\Delta\phi$ are the differences in pseudorapidity and azimuthal angle between any
 606 two considered objects. A central and a forward region of pseudorapidity are also defined
 607 such that the detector components are described as part of the *barrel* if they belong to the
 608 former or as part of the *end-caps* if they belong to the latter.

609 2.2.1 The Magnet System

610 The ATLAS magnet system, 26 m long with a 22 m diameter, generates the magnetic field
 611 needed to bend the trajectories of charged particles in order to perform momentum meas-
 612 urement. Figure 2.3a and 2.3b show the geometry of the system and its components,
 613 which are made of NbTi - superconducting material - and will be described in the follow-
 614 ing paragraphs.

615 The Central Solenoid

616 With an axial length of 5.8 m, an inner radius of 2.46 m, and an outer radius of 2.56 m, the
 617 central solenoid magnet is located between the ID and the ECAL. Its function is to bend
 618 the charged particles that go through the ID and it is aligned on the beam axis providing a
 619 2 T axial magnetic field that allows accurate momentum measurement up to 100 GeV [29].



(a) Geometry of magnet windings and tile calorimeter steel. The eight barrel toroid coils, with the end-cap coils interleaved are visible. The solenoid winding lies inside the calorimeter volume [4].

(b) Schematic view of the superconducting magnets [29].

Figure 2.3: The ATLAS magnet system.

620 The Barrel and the End-cap Toroids

621 Figure 2.3b displays the toroid magnetic system that surrounds the calorimeters. With its
 622 cylindrical shape this component consists of a barrel and two end-caps toroids, each with
 623 eight superconducting coils. The system allows accurate measurement of muon momenta
 624 using a magnetic field of approximately 0.5 T (barrel) for the central regions and 1 T (end-
 625 cap) for the end-cap regions, respectively, which bends the particles in the θ direction.

626 2.2.2 The Inner Detector

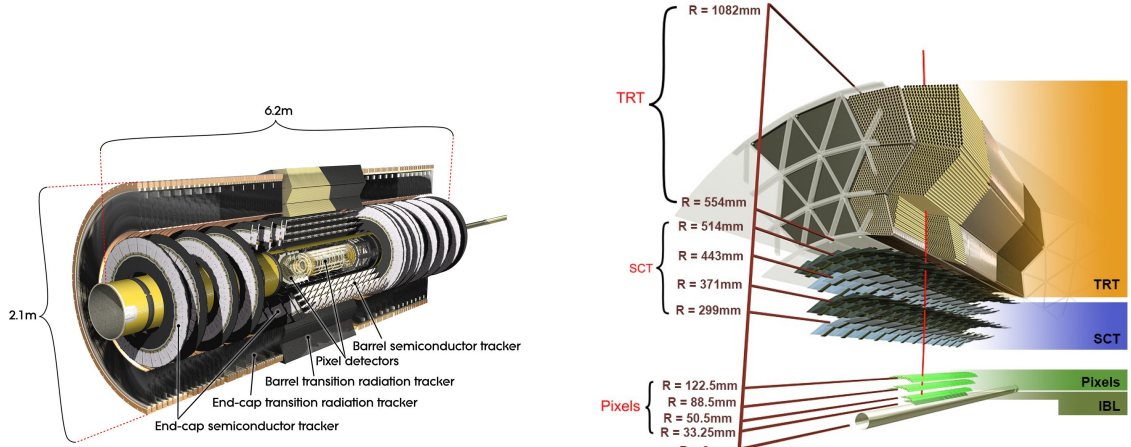
627 The Inner Detector (ID) [30] is the innermost component of the ATLAS detector i. e. the
 628 nearest sub-detector to the interaction region and it is used to reconstruct charged particle
 629 tracks used in the selection of physics objects. In fact, it allows robust track reconstruction,
 630 with accurate impact parameter resolution ($\sim 20\mu m$) and precise primary and secondary
 631 vertex reconstruction for charged particles (tracks) above 500 MeV and within $|\eta| < 2.5$.

632 The ID is comprised of independent and concentric sub-systems, which are all shown
 633 in Figure 2.4:

634 • Insertable B-Layer (IBL):

635 innermost Pixel Detector layer added during ATLAS Run 2 upgrade (2013/2014) to
 636 improve vertexing and impact parameter reconstruction;

637 • Silicon Pixel Tracker (Pixel):



(a) Overview of the ATLAS ID with labels and dimensions.

(b) Diagram of the ATLAS ID and its sub-detectors.

Figure 2.4: The ATLAS Inner Detector

made of silicon pixel layers and used mainly for reconstructing both the primary and secondary vertices in an event;

638 • SemiConductor Tracker (SCT):

639 comprised of silicon microstrip layers; thanks to its resolution ($17 \times 580 \mu\text{m}$) it can
640 accurately measure particle momenta;

641 • Transition Radiation Tracker (TRT):

642 final layer comprised of various layers of gaseous straw tube elements surrounded
643 by transition radiation material.

644 These sub-detectors will be discussed in the following sections.

645 **IBL**

646 The IBL [31] is the innermost Pixel Detector layer as shown in Figure 2.4b. It is comprised
647 of 6M channels and each pixel measures $50 \times 250 \mu\text{m}$. Its resolution is $8 \times 40 \mu\text{m}$,
648 The addition of this new layer brought a considerable improvement on the performance of the
649 Pixel Detector by enhancing the quality of impact parameter reconstruction of tracks. In
650 particular, this was achieved by improving the vertex finding efficiency and the tagging
651 of bottom-quark-initiated jets (b -jets) which, in case of a B-layer failure, can be restored
652 by the IBL. Besides these improvements, the IBL insertion allowed ATLAS to better cope
653 with high luminosity effects such as the increase in event pile-up, which leads to high
654 occupancy and read-out inefficiency.

657 Pixel

658 The Pixel detector is comprised of 1750 identical sensorchip-hybrid modules, each cover-
 659 ing an active area of 16.4×60.8 mm. The total number of modules correspond to roughly
 660 80 million semiconductor silicon pixels. The nominal pixel size is $50 \mu\text{m}$ in the ϕ direction
 661 and $400 \mu\text{m}$ in the barrel region, along the z -axis (beam axis) [32]. The reason why such a
 662 large amount of pixels is employed is justified by the need to cope with the high luminos-
 663 ity in ATLAS. The silicon pixel detector measures 48.4 cm in diameter and 6.2 m in length
 664 providing a pseudorapidity coverage of $|\eta| < 2.5$. Figure 2.4b shows the three concentric
 665 barrel layers placed at 50.5 mm, 88.5 mm and 122.5 mm respectively. Furthermore, the
 666 Pixel detector is made of six disk layers, three for each forward region, such that when a
 667 charged particle crosses the layers it will generate a signal at least in three space points.
 668 The fine granularity of such detector allows accurate measurement and precise vertex re-
 669 construction, as it provides a more accurate position measurement as a large detection
 670 area is available. In particular, it has a resolution of $10 \times 115 \mu\text{m}$.

671 SCT

672 The SCT is made of 4088 modules of silicon micro-strip detectors arranged in four con-
 673 centric barrel layers. It is mainly used for precise momentum reconstruction over a range
 674 $|\eta| < 2.5$ and it was designed for precision measurement of the position using four points
 675 (corresponding to eight silicon layers), obtained as track hits when crossing the layers.
 676 Figure 2.4b shows the structure of the SCT with its four concentric barrel layers with radii
 677 ranging from 299 mm to 514 mm and two end-cap layers. Each module has an intrinsic
 678 resolution of $17 \mu\text{m}$ in the $R - \phi$ direction and $580 \mu\text{m}$ in the z direction. As the SCT is fur-
 679 ther away from the beam-pipe than the Pixel detector, it has to cope with reduced particle
 680 density. This allows for reduced granularity maintaining the same level of performance of
 681 the Pixel detector: SCT can use ~ 6.3 million read-out channels.

682 TRT

683 The last and outermost of the sub-systems in the ID is the TRT. It is a gaseous detector
 684 which consists of 4 mm diameter straw tubes wound from a multilayer film reinforced
 685 with carbon fibers and containing a $30 \mu\text{m}$ gold plated tungsten wire in the center. The
 686 straw is filled with a gas mixture of 70% Xe, 27% CO₂ and 3% O₂ [33]. As shown in
 687 Figure 2.4b, its section consists of three concentric layers with radii ranging from 544 mm
 688 to 1082 mm, each of which has 32 modules containing approximately 50,000 straws, 1.44 m

in length, aligned parallel to the beam direction with independent read-out at both ends.
Both end-cap sections are divided into 14 wheels, with roughly 320,000 straws in the R-direction. The average 36 hits per track in the central region of the TRT allow continuous tracking to enhance pattern recognition and momentum resolution in the $|\eta| < 2.5$ region.
It also improves the p_T resolution for longer tracks.

2.2.3 The Calorimeters

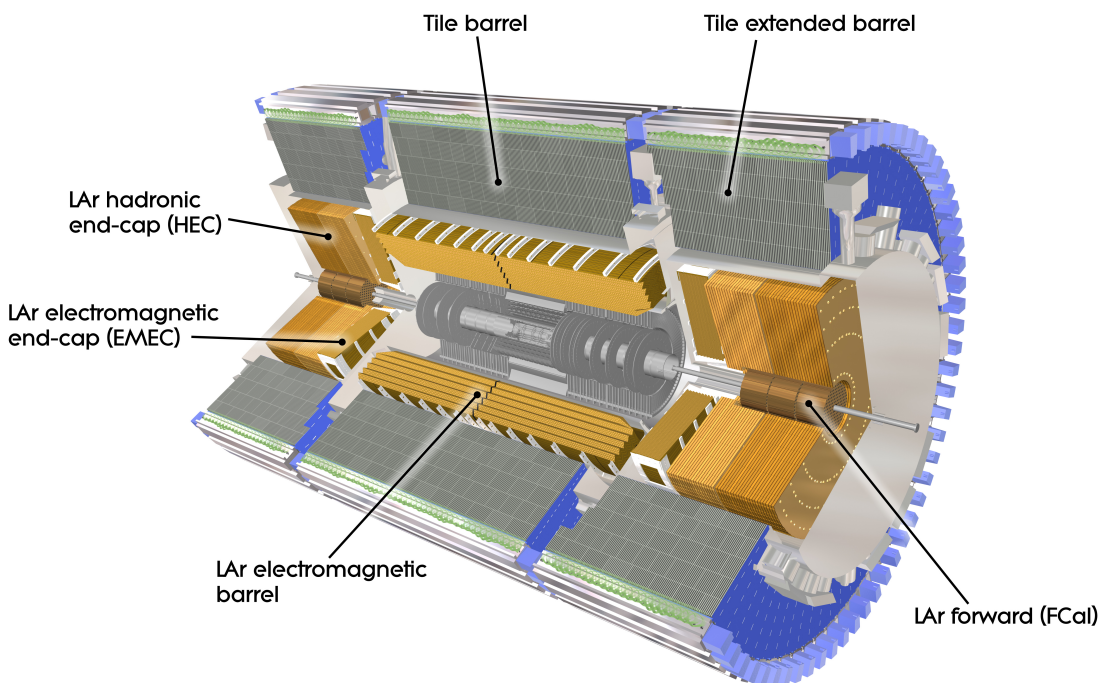


Figure 2.5: A computer generated image of the full calorimeter.

The ATLAS Calorimeter system, shown in Figure 2.5, is comprised of two main subsystems; the electromagnetic calorimeter (ECAL) and hadronic calorimeter (HCAL), which are designed to stop and measure the energy of electromagnetic-interacting and hadronic particles respectively. The combination of the two provides full coverage in ϕ and $|\eta| < 4.95$. Particles slow down and lose energy generating showers when crossing different layers. The ECAL is comprised of one barrel and two end-cap sectors employing liquid Argon (LAr). The showers hereby develop as electrons pairs which are then collected. The HCAL is also comprised of one barrel and two end-cap sectors. The sensors in the barrel of the HCAL are tiles of scintillating plastic whereas LAr is employed for the end-cap. A forward region, the closest possible to the beam, is covered by a LAr forward calorimeter (FCal). The LAr and Tile Calorimeter will be briefly discussed in the

706 following paragraphs.

707 The Liquid Argon Calorimeters

708 The ECAL is comprised of multiple layers of liquid Argon (LAr) sampler and lead ab-
709 sorber. The choice of its accordion-geometry design brought two main advantages; full
710 ϕ coverage with no non-interactive regions (no cracks); fast extraction of signals coming
711 from both front or rear end of the electrodes. It is made of two half-barrel wheels, both
712 placed in the barrel cryostat, that provide a pseudorapidity coverage up to $|\eta| < 1.475$
713 and two end-cap detectors providing $1.375 \leq |\eta| \leq 3.20$ coverage in two end-cap cryo-
714 stats. The junction between the barrel and end cap components defines the crack region
715 and any signal coming from the crack region is therefore discarded.

716 In the $|\eta| < 1.8$ region there is an additional layer, placed at the front of the calorimeter,
717 that is made of a thin (0.5 cm in the end-cap and 1.1 cm in the barrel) LAr layer with
718 no absorber [34]. This additional layer was designed to correct for the energy lost, as
719 particles enter the calorimeter, by taking a measurement just before the majority of the
720 electromagnetic shower is developed.

721 The Tile calorimeter

722 The main purpose of the hadronic calorimeter is to measure the energy of hadronic showers.
723 It is built employing steel and scintillating tiles coupled to optical fibres which are read
724 out by photo-multipliers. As shown in Figure 2.5, the HCAL is made up of three cylin-
725 ders; a central barrel, 5.64 m long covering a region $|\eta| < 1.0$, and two extended barrel,
726 2.91 m long covering a reigon $0.8 < |\eta| < 1.7$. Each cylinder is made up of 64 modules
727 and each module is in turn made up of three layers. Ultimately, the smallest section of the
728 calorimeter module is a cell with a $\Delta\phi \times \Delta\eta = 0.1 \times 0.1$ granularity for the two innermost
729 layers and $\Delta\phi \times \Delta\eta = 0.2 \times 0.1$ for the outermost one.

730 2.2.4 The Muon Spectrometer

731 The MS [35], shown in Figure 2.6, is the outermost sub-system of the whole ATLAS de-
732 tector. As such, it surrounds the calorimeters and its main function is to perform precision
733 measurement of muons momenta. The deflection of muon tracks employing large super-
734 conducting air-core toroid magnets and high-precision tracking chambers is at the heart
735 of such high precision measurement.

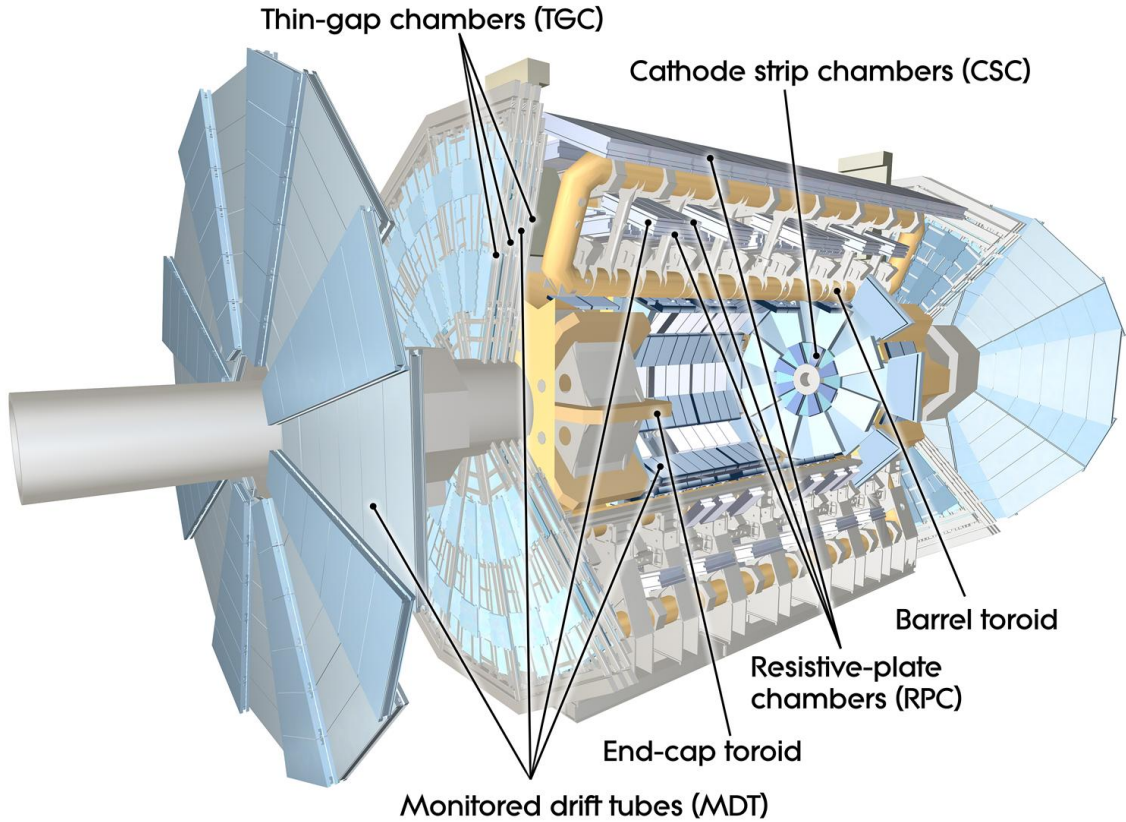


Figure 2.6: Cut-away view of the ATLAS muon system [4].

736 The MS is comprised of one large barrel toroid, covering the region $|\eta| \leq 1.4$, and
 737 two end-cap toroids, covering $1.6 < |\eta| \leq 2.7$ which are employed together to achieve the
 738 track-bending effect wanted. The magnitude of the magnetic field in the barrel, generated
 739 by eight large superconducting coils, ranges from 0.5 to 2 T.

740 Around the beam axis, three cylindrical layers make way for the chambers, placed in
 741 planes perpendicular to the beam, used to measure tracks.

742 Monitored Drift Chambers (MDTs) are employed over most of the pseudorapidity
 743 range to provide precision measurement of track coordinates in the bending direction.
 744 Cathode Strip Chambers (CSCs) are instead employed at large pseudorapidity ($2 < |\eta| <$
 745 2.7). Finally, in the end-cap regions Thin-Gap Chambers (TGCs) together with Resistive-
 746 Plate Chambers (RPCs) are dedicated to the Trigger System discussed in Section 2.3.

747 2.3 The ATLAS Trigger System

748 The ATLAS Trigger System is at the heart of data taking. It is an essential component of
 749 any nuclear or particle physics experiment since it is responsible for deciding whether or
 750 not to store an event for later study [5]. Its main function to reduce the event rate from \sim

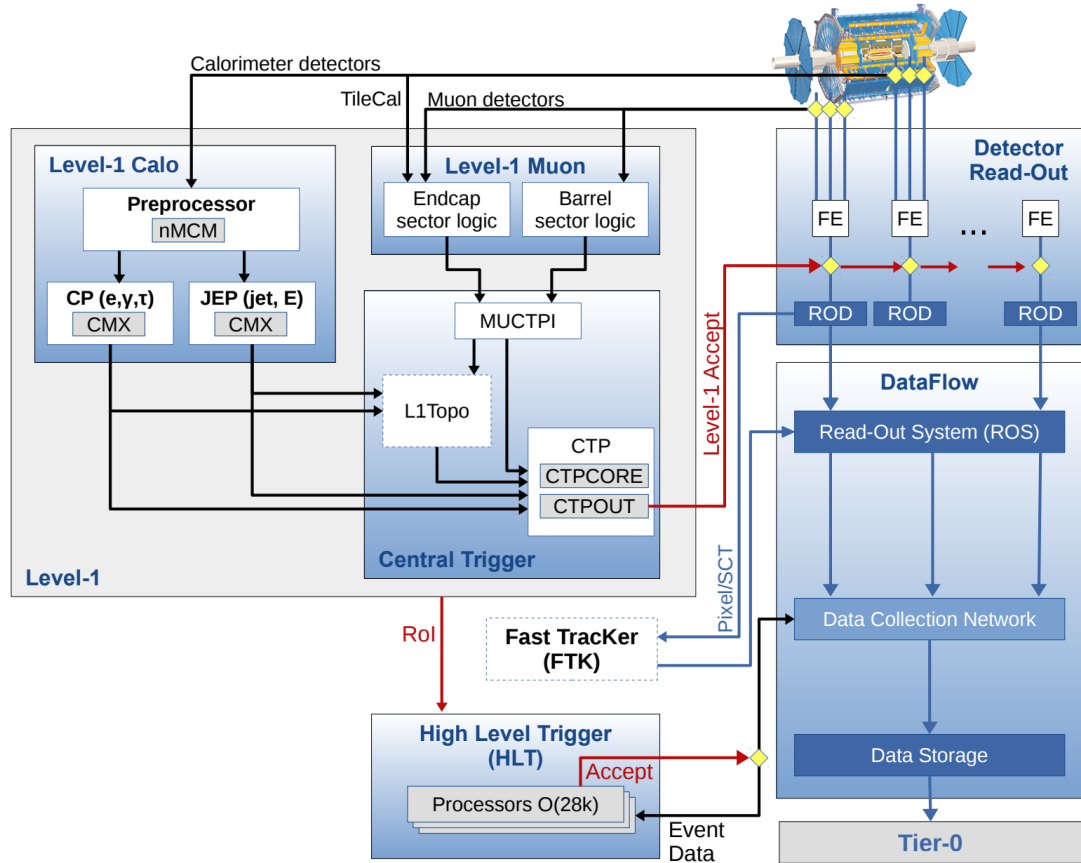


Figure 2.7: The ATLAS TDAQ system. L1Topo and FTK have not been used for the results shown in this thesis [5].

751 40 MHz¹ bunch-crossing² to ~ 200 Hz which corresponds to roughly 300 MB/s.

752 The Trigger and Data Acquisition (TDAQ) utilises a two-level system shown in Fig-
 753 ure 2.7, a first hardware-based level trigger (L1) and a software-based high-level trigger
 754 (HLT). The L1 trigger decision is formed by the Central Trigger Processor (CTP), which
 755 receives inputs from the L1 calorimeter (L1Calo) and L1 muon (L1Muon) triggers. L1 is a
 756 hardware-based system that uses information from the calorimeter and muon subdetec-
 757 tors, and defines the so-called Regions of Interest (RoIs) within the detector to be invest-
 758 igated by the next level trigger, the HLT. Additionally, a Fast TracKer (FTK) system [36]
 759 (not yet installed) will provide global ID track reconstruction at the L1 trigger rate using
 760 lookup tables stored in custom associative memory chips for the pattern recognition. The
 761 FPGA-based track fitter will perform a fast linear fit and the tracks are made available to

¹ The LHC delivers beams with a bunch-spacing of 25 ns.

² The term bunch-crossing is hereby used when referring to a collision between two bunches of protons. Since only a certain fraction of the total momentum carried by each proton contributes to the collision, an average number of interactions per bunch-crossing, $\langle \mu \rangle$ is used.

⁷⁶² the HLT. This system will allow the use of tracks at much higher event rates in the HLT
⁷⁶³ than is currently affordable using CPU systems. However, the upgrade of the ATLAS
⁷⁶⁴ trigger will not be discussed any further.

⁷⁶⁵ The ATLAS trigger system will be further discussed in Chapter [3](#).

766 3 | The ATLAS Trigger System

767 The ATLAS trigger system together with its performance will be presented in this chapter.
768 A brief introduction, about the reason behind the need of a trigger system together with
769 its implementation in ATLAS will be discussed in Section 3.1. The algorithms used for
770 the tracking in the inner detector will then be described in Section 3.2. Ultimately, meas-
771 urements of the performance of the low transverse momentum single lepton triggers and
772 medium and high transverse momentum b -jet triggers, as part of the *qualification task*¹ of
773 the author, will be discussed in Section 3.3.

774 3.1 Overview

775 In 2016 and 2017 LHC performed incredibly well delivering more than 80 fb^{-1} of pp col-
776 lisions. As previously mentioned in Section 2.3, due to storage space limitations it is not
777 feasible to save all the information about the collision after every bunch crossing, so the
778 ATLAS Trigger System is indispensable to reduce the read-out rate to a sensible value
779 without affecting the physics programme of ATLAS, e. g. discarding potentially interest-
780 ing events. A multiple-level architecture is employed to allow the trigger some more time
781 such that the identification, of an interesting event, using both software- and hardware-
782 based real-time algorithms to determine whether or not a bunch-crossing contains inter-
783 esting physics, is made possible.

784 The trigger system is configured via the so-called trigger *menu* that is meant to define
785 the trigger *chains* - usually referred to just as trigger - that start from a L1 trigger and
786 specify a sequence of reconstruction and selection steps for the specific trigger signatures
787 required in the trigger chain. Fig. 3.1 shows an illustration of an electron-trigger chain
788 used to select electrons [6].

789 The two levels will be discussed in the following sections.

¹ In order to become an ATLAS author, a person must have been an active ATLAS member for at least one year working on a technical work

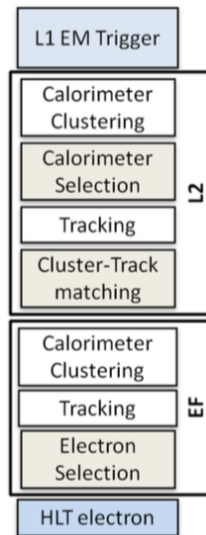


Figure 3.1: An Electron-trigger chain (from [6]).

790 3.1.1 Level 1 Trigger

791 The Level 1 (L1) trigger decision is formed by the Central Trigger Processor (CTP), based
 792 on information from the calorimeter trigger towers and dedicated triggering layers in the
 793 muon system. The CTP forms the L1 trigger decision by applying the multiplicity require-
 794 ments and prescale factors specified in the trigger menu to the inputs from the L1 trigger
 795 systems. The CTP also provides random triggers and can apply specific LHC bunch cross-
 796 ing requirements. The L1 trigger decision is distributed, together with timing and control
 797 signals, to all ATLAS sub-detector readout systems.

798 The first level, known as Level 1 (L1) trigger, is a hardware-based stage. It processes
 799 low-granularity information from the calorimeter and the muon spectrometer and iden-
 800 tifies the so-called Regions of Interest (RoIs)² before making a decision. It then feeds the
 801 next level, the high-level trigger (HLT) which will perform further investigations. L1 is im-
 802 plemented in fast custom electronics to keep the decision time around $2.5 \mu\text{s}$. Event data
 803 from other sub-systems are temporarily stored in memories whilst L1 decision is taken.

804 During the long shutdown (LS1), various upgrades were implemented in order to
 805 prepare for the expected higher rates in Run 2. A new topological trigger (L1-Topo) con-
 806 sisting of two FPGA-based (Field-Programmable Gate Arrays) processor modules was
 807 added in L1. L1-Topo [37] is fed with energy and direction information about the objects
 808 found by the L1 calorimeter and the muon trigger, which will be processed by dedicated
 809 algorithms implemented in its own FPGAs. However, due to the 100 kHz read-out rate,

² $\eta - \phi$ regions where event features have been found by the L1 selection process.

810 not all the information collected by L1-Topo will be sent to the HLT. In order to properly
811 seed the RoI-guided HLT reconstruction, specific objects in combination with the correct
812 topological criteria must be employed.

813 **3.1.2 High-Level Trigger**

814 The HLT is used to reduce the output rate down to 1 kHz and it has a \sim 200 ms average
815 decision time. Events that pass L1 trigger are then processed by the HLT using finer-
816 granularity calorimeter information, precision measurements from the MS and tracking
817 information from the ID. The HLT reconstruction can be run within RoIs identified at L1
818 or a so-called full-scan on the full detector can be performed. The track reconstruction in
819 the Inner Detector is an essential component of the trigger decision in the HLT and it will
820 be discussed more in detail in Chapter 3

821 **3.2 The tracking**

822 **3.3 Performance of HLT**

823 **3.3.1 Electrons**

824 **3.3.2 Muons**

825 **3.3.3 b -jets**

826 **4** | Event Simulation and Reconstruc-

827 **tion**

828 bla bla bla

829 **4.1 Event Simulation**

830 bla bla

831 bla bla

832 bla bla

833 bla bla

834 **4.1.1 Event Generation**

835 bla bla bla

836 bla bla bla

837 bla bla bla

838 bla bla bla

839 **4.1.2 Detector Simulation**

840 bla bla bla

841 bla bla bla

842 bla bla bla

843 **4.2 Object Reconstruction**

844 bla bla bla

845 bla bla bla

846 4.2.1 Tracks and vertices

847 bla bla bla

848 bla bla bla

849 4.2.2 Electrons

850 bla bla bla

851 bla bla bla

852 4.2.3 Muons

853 bla bla bla

854 bla bla bla

855 4.2.4 Jets

856 bla bla bla

857 bla bla bla

858 4.2.5 Missing Transverse Energy

859 bla bla bla

860 bla bla bla

861 4.2.6 Overlap Removal

862 bla bla bla

863 bla bla bla

864 **5** | Stop searches in final states with
865 jets and missing transverse en-
866 ergy

⁸⁶⁷ **6** | Results and Statistical Interpretations

⁸⁶⁸

⁸⁶⁹ **Appendix A**

Bibliography

- [1] ATLAS Collaboration, "Summary plots from the atlas standard model physics group." https://atlas.web.cern.ch/Atlas/GROUPS/PHYSICS/CombinedSummaryPlots/SM/ATLAS_a_SMSummary_TotalXsect/ATLAS_a_SMSummary_TotalXsect.png. viii, 9
- [2] C. Borschensky, M. Krämer, A. Kulesza, M. Mangano, S. Padhi, T. Plehn, and X. Portell, *Squark and gluino production cross sections in pp collisions at $\sqrt{s} = 13, 14, 33$ and 100 TeV*, *Eur. Phys. J.* **C74** no. 12, (2014) 3174, [arXiv:1407.5066 \[hep-ph\]](https://arxiv.org/abs/1407.5066). viii, 18
- [3] C. Lefèvre, *The CERN accelerator complex*, <http://cds.cern.ch/record/1260465>. ix, 22, 23
- [4] ATLAS Collaboration, *The ATLAS experiment at the CERN Large Hadron Collider*, *Journal of Instrumentation* **3** no. 08, (2008) S08003. <http://stacks.iop.org/1748-0221/3/i=08/a=S08003>. ix, 25, 30
- [5] A. Collaboration, *Performance of the ATLAS Trigger System in 2015*, *Eur. Phys. J.* **C77** (2017), [arXiv:1611.09661 \[hep-ex\]](https://arxiv.org/abs/1611.09661). ix, 30, 31
- [6] ATLAS Collaboration, *Performance of the ATLAS Trigger System in 2010*, *Eur. Phys. J.* **C72** (2012), [arXiv:1110.1530 \[hep-ex\]](https://arxiv.org/abs/1110.1530). ix, 33, 34
- [7] M. Herrero, *The Standard Model*, <https://arxiv.org/abs/hep-ph/9812242>. 3
- [8] ATLAS Collaboration, *Observation of a New Particle in the Search for the Standard Model Higgs Boson with the ATLAS Detector at the LHC*, *Phys.Lett.* **B716** (2012), [arXiv:1207.7214 \[hep-ex\]](https://arxiv.org/abs/1207.7214). 3
- [9] CMS Collaboration, *Observation of a new boson at a mass of 125 GeV with the CMS experiment at the LHC*, *Phys.Lett.* **B716** (2012), [arXiv:1207.7235 \[hep-ex\]](https://arxiv.org/abs/1207.7235). 3

- 894 [10] A. Pich, *The Standard Model of Electroweak Interactions*, arXiv:1201.0537 [hep-ph].
 895 [4](#), [7](#)
- 896 [11] K. A. Olive at al. (Particle Data Group), *Review of Particle Physics*, Chin.Phys. C **38**(9)
 897 (2014). [4](#)
- 898 [12] J. Goldstone, A. Salam and S. Weinberg, *Broken Symmetries*, Phys. Rev. **127** (1962)
 899 [965–970](#). [8](#)
- 900 [13] S. Weinberg, *Implications of Dynamical Symmetry Breaking*, Phys. Rev. **D19** (1976)
 901 [1277–1280](#). [10](#)
- 902 [14] Super-Kamiokande Collaboration, Y. Fukuda et al., *Evidence for oscillation of
 903 atmospheric neutrinos*, Phys. Rev. Lett. **81** (1998) 1562–1567, arXiv:hep-ex/9807003
 904 [hep-ex]. [10](#)
- 905 [15] SNO Collaboration, *Measurement of the Rate of $\nu_e + d \rightarrow p + p + e^-$ Interactions
 906 Produced by 8B Solar Neutrinos at the Sudbury Neutrino Observatory*, Phys. Rev. Lett.
 907 **87** (2001). [10](#)
- 908 [16] T. O. W. of the Nobel Prize.
 909 https://www.nobelprize.org/nobel_prizes/physics/laureates/2015/. [10](#)
- 910 [17] F. Jegerlehner, *The hierarchy problem of the electroweak Standard Model revisited*,
 911 arXiv:1305.6652 [hep-ph]. [12](#)
- 912 [18] A. H. Chamseddine, R. Arnowitt, and P. Nath, *Locally Supersymmetric Grand
 913 Unification*, Phys. Rev. Lett. **49** (1982) 970–974.
 914 <https://link.aps.org/doi/10.1103/PhysRevLett.49.970>. [13](#)
- 915 [19] A. Arbey, M. Battaglia, A. Djouadi, F. Mahmoudi, and J. Quevillon, *Implications of a
 916 125 GeV Higgs for supersymmetric models*, Physics Letters B **708** no. 1, (2012) 162 – 169.
 917 <http://www.sciencedirect.com/science/article/pii/S0370269312000810>. [13](#)
- 918 [20] L. Randall and R. Sundrum, *Out of this world supersymmetry breaking*, Nucl. Phys.
 919 **B557** (1999) 79–118, arXiv:hep-th/9810155 [hep-th]. [13](#)
- 920 [21] G. F. Giudice, M. A. Luty, H. Murayama, and R. Rattazzi, *Gaugino mass without
 921 singlets*, JHEP **12** (1998) 027, arXiv:hep-ph/9810442 [hep-ph]. [13](#)
- 922 [22] H. E. Haber and G. L. Kane, *The Search for Supersymmetry: Probing Physics Beyond the
 923 Standard Model*, Phys. Rept. **117** (1985) 75–263. [14](#)

- 924 [23] K. Hidaka and A. Bartl, *Impact of bosonic decays on the search for the lighter stop and*
 925 *sbottom squarks*, Phys. Lett. **B501** (2001) 78–85, arXiv:hep-ph/0012021 [hep-ph]. 14
- 926 [24] J.M. Jowett, M. Schaumann, R. Alemany, R. Bruce, M. Giovannozzi, P. Hermes, W.
 927 Hofle, M. Lamont, T. Mertens, S. Redaelli, J. Uythoven, J. Wenninger, *The 2015*
 928 *Heavy-Ion Run of the LHC*,
 929 <http://accelconf.web.cern.ch/accelconf/ipac2016/papers/tupmw027.pdf>. 21
- 930 [25] O. S. Brüuning, P. Collier, P. Lebrun, S. Myers, R. Ostojic, J. Poole and P. Proudlock,
 931 *LHC Design Report*, <https://cds.cern.ch/record/782076>. 22
- 932 [26] CMS Collaboration, *The CMS experiment at the CERN LHC*, Journal of
 933 Instrumentation **3** no. 08, (2008) S08004.
 934 <http://stacks.iop.org/1748-0221/3/i=08/a=S08004>. 22
- 935 [27] LHCb Collaboration, et. al, *The LHCb Detector at the LHC*, JINST (2008). 22
- 936 [28] ALICE Collaboration, *The ALICE experiment at the CERN LHC*, Journal of
 937 Instrumentation **3** no. 08, (2008) S08002.
 938 <http://stacks.iop.org/1748-0221/3/i=08/a=S08002>. 22
- 939 [29] A. Yamamoto, Y. Makida, R. Ruber, Y. Doi, T. Haruyama, F. Haug, H. ten Kate,
 940 M. Kawai, T. Kondo, Y. Kondo, J. Metselaar, S. Mizumaki, G. Olesen, O. Pavlov,
 941 S. Ravat, E. Sbrissa, K. Tanaka, T. Taylor, and H. Yamaoka, *The ATLAS central*
 942 *solenoid*, Nuclear Instruments and Methods in Physics Research Section A:
 943 Accelerators, Spectrometers, Detectors and Associated Equipment **584** no. 1, (2008)
 944 53 – 74.
 945 <http://www.sciencedirect.com/science/article/pii/S0168900207020414>. 24,
 946 25
- 947 [30] ATLAS Collaboration, *The ATLAS Inner Detector commissioning and calibration*, Eur.
 948 Phys. JC**70** , arXiv:1004.5293. 25
- 949 [31] ATLAS Collaboration, *ATLAS Insertable B-Layer Technical Design Report*,
 950 <https://cds.cern.ch/record/1291633>. 26
- 951 [32] G. A. et al., *ATLAS pixel detector electronics and sensors*, Journal of Instrumentation **3**
 952 no. 07, (2008) P07007. <http://stacks.iop.org/1748-0221/3/i=07/a=P07007>. 27
- 953 [33] A. Bingül, *The ATLAS TRT and its Performance at LHC*, Journal of Physics:
 954 Conference Series **347** no. 1, (2012) 012025.

-
- 955 <http://iopscience.iop.org/article/10.1088/1742-6596/347/1/012025/meta>.
- 956 27
- 957 [34] ATLAS Collaboration, *ATLAS liquid-argon calorimeter: Technical Design Report*,.
- 958 <https://cds.cern.ch/record/331061>. 29
- 959 [35] ATLAS Collaboration, *ATLAS muon spectrometer: Technical design report*,.
- 960 <https://cds.cern.ch/record/331068>. 29
- 961 [36] ATLAS Collaboration, *Fast TracKer (FTK) Technical Design Report*,.
- 962 <https://cds.cern.ch/record/1552953>. 31
- 963 [37] E. Simoni, *The Topological Processor for the future ATLAS Level-1 Trigger: from design to commissioning*, [arXiv:1406.4316](https://arxiv.org/abs/1406.4316). 34
- 964